https://doi.org/10.5194/egusphere-2026-3065
Preprint. Discussion started: 24 June 2026

Climate and Carbon Cycle Responses to a 21st century AMOC Collapse under a 2°C Stabilization Pathway

Thomas L. Frölicher[1,2], Patrick Maier[1], Friedrich A. Burger[1,2], Yona Silvy[1,2], Didier Swingedouw[3], Urs Hofmann Elizondo[1,2], and Manon Berger[1,2]

[1]Climate and Environmental Physics, Physics Institute, University of Bern, Switzerland
[2]Oeschger Centre for Climate Change Research, University of Bern, Switzerland
[3]Environnements et Paléoenvironnements Océaniques et Continentaux (EPOC), University Bordeaux, CNRS, France

Correspondence: Thomas L. Frölicher (thomas.froelicher@unibe.ch)

Abstract

The Atlantic Meridional Overturning Circulation (AMOC) is a key component of the climate system, yet the climate and carbon cycle responses to a collapse under emission pathways consistent with the Paris Agreement remain poorly understood. Using the comprehensive GFDL ESM2M Earth System Model with the Adaptive Emissions Reduction Approach, we impose a freshwater-induced strong AMOC weakening to 20% of its preindustrial strength, initiated in year 2026 and achieved within 60 years. The counterfactual simulations without freshwater hosing otherwise follow a pathway in which global warming stabilizes at 2°C and the AMOC weakens only modestly and partially recovers. Relative to the 2°C scenario without AMOC collapse, a strong AMOC weakening cools global mean surface air temperature by -0.8°C (5-member ensemble range: -0.7 to -0.9) by 2171-2200, offsetting 40% of global warming. Pronounced cooling is simulated in the North Atlantic region, reaching up to -5.4°C (-8.0 to -3.3) in winter over Iceland relative to 1861-1900 conditions. The global cooling is primarily driven by larger negative feedback from clouds, driven by an increase in low-level clouds in the North Atlantic region, with smaller contributions from enhanced global ocean heat storage and reduced atmospheric CO_2. The total ocean heat content increases by an additional 488 ZJ (442-531), primarily south of 20°N, associated with reduced northward heat transport and enhanced heat uptake in the North Atlantic. The additional heat increases global thermosteric sea level rise by an additional 10% (8–12), with enhanced rise in the western and tropical North Atlantic and northern Indian Ocean, but pronounced reductions in the eastern North Atlantic. Atmospheric CO_2 declines by 13 ppm due to anomalous land carbon uptake of 44 GtC (33–53), dominated by enhanced carbon storage in the Amazon region under cooler and wetter conditions. In contrast, global ocean carbon storage decreases by 14 GtC, mainly north of 20°N. The AMOC-induced cooling temporarily breaks the near-linear relationship between cumulative CO_2 emissions and warming, increasing the remaining emission budget for limiting warming to 2°C by 63% (54–72). Compared to identical freshwater forcing under preindustrial conditions, the surface temperature, ocean heat content, and sea-level responses to an AMOC collapse are substantially damped in a 2°C world, indicating reduced climate sensitivity to AMOC collapse in a warmer world. These results demonstrate that a strong AMOC weakening would

https://doi.org/10.5194/egusphere-2026-3065
Preprint. Discussion started: 24 June 2026

profoundly alter the climate–carbon cycle system and underscore the importance of explicitly accounting for AMOC risks in long-term climate assessments.

1 Introduction

The Atlantic Meridional Overturning Circulation (AMOC) is a key component of the global ocean circulation (Broecker, 1992; Fox-Kemper et al., 2021; University of Potsdam and Rahmstorf, 2024). By transporting warm, saline waters northward and returning cold deep waters southward, it redistributes heat and carbon and ventilates the deep ocean (Ganachaud and Wunsch, 2000; Sabine et al., 2004). Through these processes, the AMOC exerts a strong influence on regional and global climate (e.g., Manabe and Stouffer, 1995; Rahmstorf, 2002; Buckley and Marshall, 2016)

Climate models consistently project a weakening of the AMOC over the 21st century in response to greenhouse gas forcing (Weijer et al., 2020; Portmann et al., 2026). This weakening is primarily driven by ocean warming and increasing freshwater input from precipitation and runoff, and sea-ice melt, which enhance upper ocean stratification in the deep water formation regions, thereby suppressing convection. Although the IPCC Sixth Assessment Report assessed the likelihood of an abrupt AMOC collapse before 2100 as low (medium confidence; Fox-Kemper et al. (2021)), CMIP6 models indicate that a collapse of the buoyancy driven AMOC can occur beyond 2100 (Drijfhout et al., 2025). Structural limitations of many CMIP-class models, including biases in the Atlantic freshwater budget, and non interactive ice-sheets may contribute to an overly stable simulated AMOC (Liu et al., 2017; Arumí-Planas et al., 2024; Vanderborght et al., 2025; Dijkstra and Van Westen, 2024; Portmann et al., 2026).

Paleoclimate evidence suggests that the AMOC has rapidly changed from a strong to a weak stable state multiple times in the past, often coinciding with abrupt climate shifts and large-scale reorganizations of the Earth system (Rahmstorf, 2002; Clark et al., 2002; Lynch-Stieglitz, 2017; Gerber et al., 2025). Notable examples include the Younger Dryas during the last deglaciation, and Heinrich and Dansgaard–Oeschger events during the last glacial period (Heinrich, 1988; Dansgaard et al., 1993). These reorganizations were accompanied by rapid cooling across the North Atlantic, widespread shifts in global precipitation patterns, substantial impacts on terrestrial and ocean carbon storage and associated changes in atmospheric CO_2 (Broecker, 2006). The paleo record thus provides strong evidence that AMOC disruptions can induce large-scale and abrupt changes in the coupled carbon cycle-climate system.

Model simulations indicate that a substantial AMOC weakening or collapse would reduce northward ocean heat transport and generate pronounced climate anomalies. These include strong cooling in the North Atlantic region (Bellomo and Mehling, 2024; Liu et al., 2020), dynamical and total sea level changes (Volkov et al., 2023; Howard et al., 2024; Van Westen et al., 2026), altered ocean heat uptake (Knutti and Stocker, 2000; Rugenstein et al., 2016; Dijkstra and van Westen, 2025), and shifts in atmospheric circulation and tropical precipitation belts (Swingedouw et al., 2009; Drijfhout, 2015; Winton et al., 2013; Liu et al., 2020, 2017; van Westen et al., 2024; Ben-Yami et al., 2024; Orihuela-Pinto et al., 2022; Saini et al., 2025). Recent simulations indicate that temperatures in northwestern Europe could decline by up to about 15°C under AMOC-collapsed conditions, accompanied by changes in cold extremes (van Westen et al., 2024; van Westen and Baatsen, 2025; Meccia et al.,

https://doi.org/10.5194/egusphere-2026-3065
Preprint. Discussion started: 24 June 2026

2023, 2025), while the Southern Hemisphere may experience anomalous warming (Pontes and Menviel, 2024) due to interhemispheric heat redistribution. Beyond physical climate impacts, an AMOC collapse could also affect terrestrial and ocean carbon storage through changes in temperature, ocean circulation, and biogeochemical processes (Swingedouw et al., 2007a; Bozbiyik et al., 2011). However, previous modeling studies show divergent atmospheric CO_2 responses, reflecting uncertainties in carbon–climate feedbacks and circulation changes (Scholze et al., 2003; Obata, 2007; Swingedouw et al., 2007a; Bozbiyik et al., 2011; Gottschalk et al., 2019; Schaumann and Alastrué de Asenjo, 2025).

Despite growing interest, substantial uncertainties remain regarding the consequences of an AMOC collapse in a warming world. Many modeling studies investigated AMOC shutdowns under preindustrial or glacial boundary conditions (Vellinga and Wood, 2002; Menviel et al., 2008; Bozbiyik et al., 2011; Jackson et al., 2015; Orihuela-Pinto et al., 2022; van Westen et al., 2024; Ma et al., 2024), limiting their transferability to a climate system already altered by anthropogenic forcing. The impacts of AMOC weakening are strongly state-dependent and interact nonlinearly with background warming (Vellinga and Wood, 2008; Kageyama et al., 2024; Bellomo and Mehling, 2024). Only a few studies have examined a collapse of AMOC superimposed on ongoing global warming. These studies typically focus on regional responses such as European temperature extremes (van Westen and Baatsen, 2025) and European hydroclimate (Van Westen et al., 2025), following highly idealized future warming scenarios (Swingedouw et al., 2007b; Bellomo and Mehling, 2024), or are based on coarse-resolution climate models (Drijfhout, 2015). Moreover, many previous studies did not include fully interactive carbon–climate interactions, preventing a comprehensive assessment of how an AMOC collapse would affect atmospheric CO_2, the transient climate response to cumulative emissions, and the remaining emission budget (Drijfhout, 2015; Liu et al., 2020; van Westen et al., 2024; Van Westen et al., 2026). An exception is the recent Earth system modeling study by Boot et al. (2024), who examined the carbon cycle responses to AMOC weakening under anthropogenic warming. They showed that strong AMOC weakening under low- and high-emission scenarios can lead to modest increases in atmospheric CO_2 driven by changes in oceanic and terrestrial carbon fluxes. However, their analysis did not explicitly assess collapse conditions within an emission-driven framework designed to quantify implications for the remaining emission budget, nor did it systematically explore the sensitivity of the response to background climate state. A systematic assessment of the climatic and carbon cycle consequences of a collapsed AMOC under emission-driven warming is therefore still lacking.

To address these gaps, we use the fully coupled Earth System Model GFDL ESM2M in emission-driven mode with interactive land and ocean carbon cycles to investigate the global and regional climate and carbon cycle responses to a present-day AMOC transition to a collapsed state. Using idealized freshwater hosing beginning in 2026, we induce a collapse within the first 100 years under an emissions pathway consistent with limiting global warming to 2°C above preindustrial levels. While the hosing is not intended to represent a realistic freshwater perturbation, it provides a controlled framework to assess the consequences of a collapse within a transient, warming climate. In contrast to most previous studies, our simulations are fully emission-driven and include interactive land and ocean carbon cycles, allowing carbon–climate feedbacks to evolve dynamically following an AMOC collapse. This framework enables us to quantify not only the physical climate response, but also the associated changes in carbon storage, atmospheric CO_2, and implications for the transient climate response and remaining emission budget under ongoing anthropogenic warming.

https://doi.org/10.5194/egusphere-2026-3065
Preprint. Discussion started: 24 June 2026

2 Methods

2.1 Earth System Model GFDL ESM2M

We use the comprehensive global coupled carbon–climate model GFDL ESM2M (Dunne et al., 2012, 2013), developed by NOAA's Geophysical Fluid Dynamics Laboratory (GFDL). Based on CM2.1 (Delworth et al., 2006), ESM2M couples the ocean (MOM4p1), atmosphere (AM2), land (LM3.0), and sea ice (including iceberg dynamics) components. MOM4p1 (Griffies et al., 2009) simulates ocean physics on a 1° horizontal grid, refined to 1/3° near the equator, with 50 vertical levels and a tripolar grid north of 65°N. Ocean biogeochemistry is represented by TOPAZv2.0, which simulates the cycles of key elements (C, P, Si, N, Fe, O_2, alkalinity and lithogenic material) using 30 prognostic tracers. AM2 (Anderson et al., 2004) resolves atmospheric processes at 2°×2.5° with 24 vertical levels. LM3.0 (Shevliakova et al., 2009) simulates water, energy, and carbon cycles, multi-layer soil and snow dynamics, and vegetation processes. The sea ice model (Winton, 2000) runs on the same grid as MOM4p1. GFDL ESM2M does not include a dynamic ice sheet component.

The GFDL ESM2M is a widely used Earth system model that participated in the Coupled Model Intercomparison Project Phase 5 (CMIP5, Taylor et al. (2012)). It realistically captures large-scale physical and biogeochemical patterns and variability (Dunne et al., 2012, 2013). Of particular importance to this study, the model performs well in simulating ocean heat and carbon uptake and key aspects of the global carbon cycle (Dunne et al., 2013; Bopp et al., 2013; Frölicher et al., 2015; Bronselaer et al., 2017; Séférian et al., 2020; Burger et al., 2022). The simulated AMOC strength at 26°N of 18.7 Sv (18.4 to 19.2) averaged over 2004 to 2020 is in good agreement with the observed mean of 17 $\pm$ 0.9 Sv from the RAPID array over the same time period (Moat, Ben I et al., 2025) (see Fig. 2a). In addition, the simulated AMOC decreases of 3.8 Sv over the historical period is in good agreement with the suggested 3 Sv weakening of the AMOC since the mid-twentieth century based on proxy reconstructions (Caesar et al., 2018).

2.2 Simulations

We conducted a suite of four different global warming simulations (Table 1) to examine the impacts of a collapse and recovery of the AMOC on the Earth system under 2°C global warming stabilization pathways (Table 1). In addition, we also conducted a hosing experiment branched from a preindustrial control simulation to investigate the state dependence of the Earth system response to a collapse of the AMOC. Each set of simulations consists of five perturbed initial condition ensemble members unless stated otherwise. The ensemble of 5 members was generated by perturbing the temperature on the 1st of January 1861 by the order 10^{-5}°C at a grid cell at the surface of the Weddell Sea (Frölicher et al., 2020).

Name	Description	Simulated Years
2°C-ref	Reference 2 °C stabilization; 5-members	1861–2200
2°C-hos-Eref	CO_2 emissions from 2°C-ref including 0.3 Sv hosing; 5-members	2026–2200
2°C-hos-Eadapt	2 °C stabilization including 0.3 Sv hosing; 5-members	2026-2200

https://doi.org/10.5194/egusphere-2026-3065
Preprint. Discussion started: 24 June 2026

2°C-r100-Eref	Branched from 2°C-hos-Eref, with hosing stopped in 2126, 1-member	2126–2200
piControl	Preindustrial conditions, 5-members	1–340
piControl-hos	Preindustrial conditions with 0.3 Sv hosing, 5-members	1–175

Table 1: **Overview of the emission-driven reference and freshwater hosing simulations performed with GFDL ESM2M.** The 2°C-reference run represents a stabilization pathway that limits warming to 2°C above preindustrial levels. "Eref" experiments use emissions from this reference simulation, whereas "Eadapt" simulations adjust emissions using AERA to maintain the 2°C target. Freshwater hosing (0.3 Sv) in the future scenarios begins in 2026. In the r100 experiment, hosing is terminated after 100 years (i.e. in 2126). Preindustrial control simulations and corresponding hosing runs (0.3 Sv starting in year 1) are also included to assess state-dependency. The total simulation length or simulation period is listed in the final column.

The reference simulation *2°C-ref* follows historical fossil fuel CO_2 emissions from 1861 to 2025. From 2026 onward, fossil fuel CO_2 emissions are adjusted using the Adaptive Emission Reduction Approach (AERA) (Terhaar et al., 2022) to stabilize global surface air temperature (GSAT) at 2°C by 2100. AERA updates the allowable future fossil-fuel CO_2 emissions every five years based on the current warming level and the remaining CO_2 forcing equivalent (CO_2-fe) emission budget estimated by the transient climate response to cumulative CO_2-fe emissions (Terhaar et al., 2022). Non-CO_2 forcing agents, as well as land-use and land-cover changes, follow historical conditions from 1861 to 2005 and RCP2.6 thereafter until 2100, and are held constant after 2100 (Silvy et al., 2024; Thomas et al., 2022). The simulated ensemble mean warming of 1.20 °C (ensemble range: 1.13 to 1.30; 2015-2024 relative to preindustrial) agrees well with the observed value of 1.24°C (Forster et al., 2025). The second set of five-member ensemble simulations, *2°C-hos-Eref*, follows the same non-CO_2 forcing and CO_2 emissions as *2°C-ref*, but imposes a uniform freshwater input of 0.3 Sv into the North Atlantic and Arctic Ocean from 2026 onward (see Section 2.3), to induce a strong weakening of the AMOC. Throughout the manuscript, we define a "collapse" of the AMOC as an approximately 80% reduction in the annual-mean AMOC strength at both 26.5°N and 48°N relative to the preindustrial control climatology (22.5 Sv at 26.5°N and 23.5 Sv at 48°N). With the *2°C-ref* experiment, we can isolate the climate and carbon cycle changes of an AMOC collapse under an emission pathway compatible with 2°C global warming. The third set of five-member ensemble simulations, *2°C-hos-Eadapt*, includes the same freshwater forcing, but AERA dynamically adjusts fossil-fuel CO_2 emissions to stabilize GSAT at 2°C. This setup allows the assessment of the Earth system state and remaining emission budget in a 2°C world with a collapsed AMOC. The fourth (*2°C-r100-Eref*) simulation with one ensemble member branches from the *2°C-hos-Eref* hosing simulation, with freshwater input stopped after 100 years in year 2126, allowing the AMOC to recover eventually and to investigate reversibility. Our primary analysis focuses on the *2°C-ref* and *2°C-hos-Eref*, while the other simulations are discussed where relevant.

To quantify the influence of the background climate state of an AMOC-collapse impact on key climate and carbon cycle metrics, we conducted an additional five-member freshwater hosing ensemble under preindustrial background forcing (*piControl-hos*; Table 1). We use the same hosing amplitude (0.3 Sv) and spatial pattern as in 2°C-hos-Eref.

https://doi.org/10.5194/egusphere-2026-3065
Preprint. Discussion started: 24 June 2026

2.3 Freshwater Hosing

To induce a strong weakening of the AMOC in GFDL ESM2M, we apply a uniform freshwater flux of 0.3 Sv, following the NaHosMIP protocol (Jackson et al., 2023). The freshwater is added to the surface grid cells over the North Atlantic north of 50°N, extending through the Arctic Ocean and the Bering Strait north of 66°N (Fig. 1a). The freshwater is added as a real freshwater flux and not as a virtual salt flux. A volume compensation is not applied to conserve salt or global salinity drifts. The freshwater hosing begins in 2026 for the future scenarios (Fig. 1b). A freshwater flux of 0.3 Sv was selected because it causes a reduction of the AMOC strength by around 80% relative to preindustrial conditions in this model, thereby producing a collapsed state. Smaller fluxes result only in a partial weakening. For example, a 0.15 Sv hosing reduces the AMOC by only 40–50% in a preindustrial control simulation (Fig. B1).

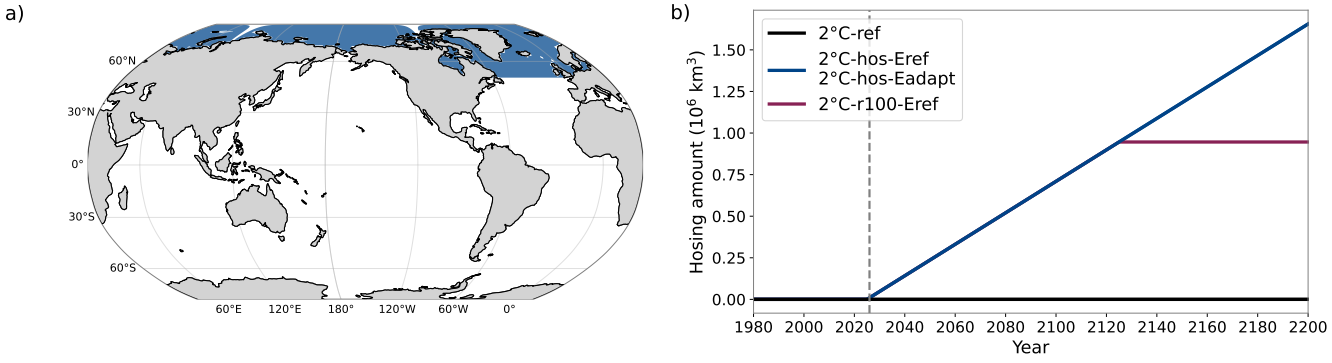

Figure 1. Uniform freshwater hosing field and cumulative input over time. (a) Spatial distribution of the uniform freshwater flux applied in the hosing experiments. (b) Time-integrated freshwater flux for all simulations. Units are in 10^6 km^3.

The applied freshwater hosing is spatially uniform, in contrast to the more localized freshwater inputs observed, which mainly originate from Greenland Ice Sheet (GIS) melt, sea-ice loss, and river runoff. For context, a continuous flux of 0.3 Sv sustained over 100 years would correspond to roughly 34% of the total GIS volume, far exceeding present-day melt rates of about 0.01 Sv observed during 2006–2018 (IPCC AR6 WGI, 2023). Even under strong future warming scenarios, projected GIS melt rates are expected to reach only about 0.06 Sv by 2100 (Glaude et al., 2024). Hence, the imposed hosing rate constitutes an unrealistic freshwater perturbation, and its spatially broad application distributes freshwater far more widely than under realistic meltwater fluxes. Nevertheless, the goal of this study is not to reproduce realistic freshwater forcing, but rather to examine the consequences of a very strong AMOC weakening, which cannot be entirely ruled out due to string model biases in CMIP6, on the coupled carbon cycle-climate system.

https://doi.org/10.5194/egusphere-2026-3065
Preprint. Discussion started: 24 June 2026

2.4 Analysis Methods

2.4.1 Calculation of AMOC and thermosteric sea level rise

The AMOC strength is calculated as the vertical maximum between 500 m and 5500 m (seafloor in ESM2M) of the meridional overturning streamfunction in the Atlantic:

$$AMOC(y) = \max_{z' \in [500\,\mathrm{m}, 5500\,\mathrm{m}]} \left(- \int_{5500\,\mathrm{m}}^{z'} \int_{x_E}^{x_W} v(x,y,z)\, dx dz \right), \tag{1}$$

where y denotes latitude, x_E and x_W are the eastern and western basin boundaries, and $v(x,y,z)$ is the meridional velocity. The velocity includes contributions from resolved advection as well as parameterized mesoscale and submesoscale eddies (Mcwilliams et al., 1990; Fox-Kemper et al., 2011). The depth integration begins at 500 m to exclude most of the wind-driven circulation. For consistency with observation and previous model analyses (Jackson et al., 2023; Romanou et al., 2023), we evaluate the AMOC strength predominantly at 26.5°N and 48°N.

The thermosteric sea level rise ($\eta_{\text{thermosteric}}$) is calculated from the temperature-driven density changes, while holding salinity and pressure fixed at their preindustrial values. We apply a first-order Taylor expansion of the grid cell height $z = \frac{m}{\rho A}$ to estimate changes in cell height resulting from thermally induced density variations relative to preindustrial conditions. For each water column, the thermosteric sea level rise is then computed as the vertical integral of the corresponding layer thickness changes (Richter et al., 2013; Palter et al., 2014, 2018; Griffies et al., 2016; Lacroix et al., 2024; Van Westen et al., 2026):

$$\eta_{\text{thermosteric}} = \int \frac{\rho_{\text{piC}} - \rho(\Theta, S_{\text{piC}}, p_{\text{piC}})}{\rho_{\text{piC}}} \mathrm{d}z. \tag{2}$$

Here, in-situ density ρ is calculated following Jackett et al. (2006), θ denotes potential temperature, S salinity, and p pressure. The subscript "piC" refers to preindustrial control climatological mean.

2.4.2 Surface air temperature decomposition

To decompose the drivers of the global surface air temperature response to an AMOC collapse, we apply a framework that separates the contributions of individual Earth system feedbacks to the global temperature change. It is based on the energy balance model of Gregory et al. (2004) for surface air temperature changes. From this framework - explained in Appendix A - the temperature difference δT between the hosing simulations (e.g., *2°C-hos-Eref*) and the reference simulations (*2°C-ref*) can be decomposed as:

$$\delta T = \delta T_P + \delta T_A + \delta T_W + \delta T_C + \delta T_N + \delta T_F. \tag{3}$$

Here, δT_P represents the contribution from static Planck response to increase in greenhouse gases, δT_A the contribution from changes in the surface albedo feedback (e.g. decrease in albedo of the Earth when sea ice is melting), δT_W the contribution from changes in the combined water vapor and lapse rate feedbacks, δT_C the contribution from changes in cloud feedbacks

https://doi.org/10.5194/egusphere-2026-3065
Preprint. Discussion started: 24 June 2026

(e.g. changes in cloud properties with warming), δT_N the contribution from variations in top-of-atmosphere net radiation (or Earth Energy Imbalance, which is dominated by ocean heat uptake), and δT_F the contribution from changes in atmospheric CO_2 forcing. The decomposition assumes linear additivity of feedback contributions and is therefore interpreted diagnostically rather than as a strict attribution. Because dedicated online radiative perturbation experiments are computationally prohibitive in a fully coupled Earth system model, the decomposition relies on the archived top-of-atmosphere radiative fluxes (including clear-sky diagnostics), which allows an approximate separation of feedback contributions. The exact definition of the different terms is provided in Appendix A.

2.4.3 Heat and ocean carbon budgets, and significance tests

We calculate the heat budget for both the ocean and atmosphere. Ocean heat content, referenced to 0°C, is calculated by multiplying the potential temperature (in °C) with the specific heat capacity of water and the model's constant reference density and integrating this product over the ocean volume. Because the geothermal heat flux is constant over time, it does not contribute to differences between hosing and non-hosing experiments (e.g., Fig. 5). The net surface atmosphere-ocean heat flux includes radiative fluxes (shortwave and longwave), turbulent fluxes (sensible and latent heat), and additional heat flux contributions associated with phase changes and mass exchange processes, including melting of frozen precipitation and calved ice, frazil ice formation, runoff, precipitation minus evaporation, and iceberg calving. Ocean heat transport is diagnosed as the residual of the time-integrated net atmosphere-ocean surface heat flux and ocean heat content. Analogously, atmospheric heat transport is diagnosed as the residual between the time-integrated net top-of-atmosphere radiative imbalance and the time-integrated net atmosphere–ocean heat exchange. The atmospheric heat storage in the atmosphere is considered to be negligible in comparison to the the ocean heat storage.

Ocean inorganic carbon content is calculated by multiplying inorganic carbon concentration (in $\mathrm{mol\,kg^{-1}}$) with the molar mass of carbon and the model's constant reference density and integrating it over the ocean volume. It changes through air-sea CO_2 exchange, inflow of carbon through river runoff, and the carbon exchange with organic carbon reservoirs, including ocean sediments. Again, the ocean transport of inorganic carbon is diagnosed as the residual between the time-integrated sum of air-sea CO_2 exchange, river carbon influx, and organic carbon reservoir exchange, and the ocean inorganic carbon content.

To assess whether simulated local changes associated with the AMOC collapse differ significantly from those in the reference simulations, we apply a two-sided t-test at the 5% significance level (Wilks, 2011). The test is applied to the 30-year mean (2171–2200) of each ensemble member, resulting in five independent samples per experiment.

3 Results

3.1 AMOC response to freshwater hosing

The imposed freshwater forcing causes a rapid and persistent weakening of the AMOC in the 2°C emission pathway simulation (*2°C-hos-Eref*), in stark contrast to the modest changes simulated under 2°C stabilization without hosing (*2°C-ref*; Figs. 2a, b;

https://doi.org/10.5194/egusphere-2026-3065
Preprint. Discussion started: 24 June 2026

Fig. B2). In the *2°C-hos-Eref* experiment, the AMOC declines sharply following the onset of hosing (Fig. 2a), decreasing from about 18.6 Sv (ensemble range: 17.6-19.7) to 12.9 Sv (12.0-13.5) between 2026 and 2045 at 26.5°N and to 7.0 Sv (6.2-8.0) by 2085. After 2085, the rate of weakening slows, with the AMOC declining by an additional 2 Sv and stabilizing at a persistently weak state of 5.1 Sv (4.5–5.6) during 2171–2200 at 26.5°N. This corresponds to an approximately 80% reduction relative to the preindustrial control climatology. Although the freshwater forcing remains constant throughout the simulation, the reduced weakening rate after the mid-21st century suggests the establishment of a quasi-equilibrium state under sustained surface freshening. The AMOC at 48°N exhibits a similar temporal evolution, with a slightly stronger initial decline to 11.5 Sv (10.1-13.0) by 2045 and 5.8 Sv (4.9-7.3) by 2085, followed by slightly lower values during 2171–2200 (Fig. 2b).

In contrast, the *2°C-ref* simulation shows only a moderate transient weakening of the AMOC under greenhouse gas forcing alone. At 26.5°N, the ensemble mean AMOC reaches a minimum of 16.5 Sv in 2081, while at 48°N the minimum of 15.8 Sv occurs around 2074 (Figs. 2a,b). Thereafter, the AMOC gradually recovers and remains approximately 10% below preindustrial levels by 2200. The overturning cell in *2°C-ref* becomes shallower relative to preindustrial conditions (Fig. B2), indicating a structural adjustment to warming and stratification but far from an AMOC collapse.

When freshwater forcing is terminated after 100 years in 2126 in the *2°C-r100-Eref* experiment, the AMOC recovers, indicating that the hosing-induced weakening is largely reversible under this stabilization pathway. Following the cessation of freshwater input, the AMOC strengthens at a rate of approximately 1.8 Sv per decade at 26.5°N and 1.7 Sv per decade at 48°N and approaches values only slightly below those of *2°C-ref* by 2200 (Figs. 2a,b). This centennial-scale recovery suggests that, in this model and climate state, the weakened AMOC does not enter an irreversible collapsed regime. However, recovery behavior is model-dependent; Jackson et al. (2023) showed that only about half of CMIP-class models exhibit recovery after freshwater hosing is removed in preindustrial simulations.

Overall, the hosing experiments produce a sustained collapse of the AMOC in a warming world, providing a physically consistent framework for assessing the resulting climate and carbon cycle responses.

3.2 Temperature response to AMOC collapse

The AMOC collapse in the *2°C-hos-Eref* experiment substantially alters the trajectory of global surface air temperature (GSAT) relative to the 2°C stabilization pathway (Fig. 2c,d). Immediately after the onset of freshwater hosing in 2026 and the associated weakening of the AMOC, GSAT begins to decline slightly despite ongoing CO_2 emissions (Fig. 2c). The lowest temperature occurs around 2050, when GSAT reaches approximately 1.0 °C above 1861-1900 conditions, before gradually increasing again as radiative forcing continues to rise (Fig. 7a).

Relative to the *2°C-ref* simulation, the AMOC collapse induces a sustained global cooling that evolves in three distinct phases: (i) an initial rapid cooling concurrent with the AMOC decline, (ii) a quasi-stable period with an approximately constant temperature offset, and (iii) renewed cooling during the prolonged weak-AMOC state (Fig. 2d; dark blue line). Around 2060, GSAT is lower by -0.61 °C (-0.52 to -0.77) compared to *2°C-ref*. The temperature difference remains close to -0.6 °C until the mid-22nd century. After approximately 2150, cooling intensifies again as the AMOC remains persistently weak, reaching -0.83 °C (-0.69 to -0.94) during 2171–2200. Overall, a sustained AMOC collapse reduces GSAT by about 0.8 °C relative to

https://doi.org/10.5194/egusphere-2026-3065
Preprint. Discussion started: 24 June 2026

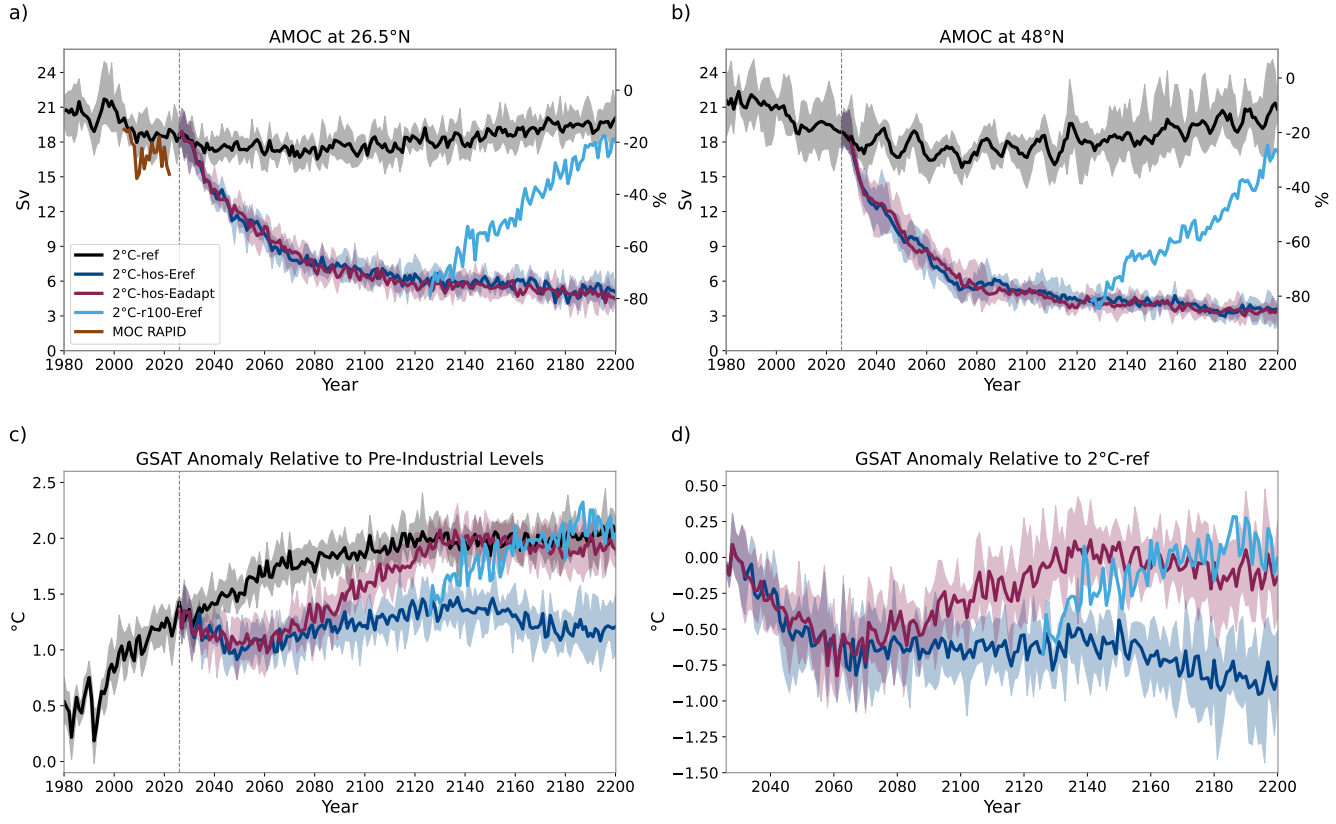

Figure 2. AMOC strength and global surface air temperature response to freshwater hosing. The AMOC strength and surface air temperature response of the hosing scenarios *2°C-hos-Eref* & *2°C-host-Eadapt*, the recovery scenario *2°C-r100-Eref*, and the *2°C-ref* simulation. (a) Annual mean AMOC strength at 26.5°N, including observations from the RAPID-MOCHA-WBTS array (Moat, Ben I et al., 2025). (b) Annual mean AMOC strength at 48°N. The right-hand axis in (a) and (b) shows the percentage deviation from the mean AMOC strength in the *piControl* simulation at the respective latitude. (c) Global annual mean surface air temperature anomaly relative to preindustrial (1861-1900). The gray shading at 2 °C represents the AERA temperature target range of ±0.2 °C. (d) Global surface air temperature difference of the hosing experiments relative to *2°C-ref*. Shading indicates the ensemble member range. The vertical dotted line marks the start year (2026) of the future simulations.

a 2°C stabilization pathway without hosing. In our model, the AMOC-induced cooling offsets roughly 40% of the targeted 2°C warming, maintaining late-22nd century temperatures near 1.1–1.2 °C above preindustrial levels, comparable to recent observed warming levels.

In the *2°C-hos-Eadapt* experiment, AERA compensates for AMOC-induced cooling by allowing higher fossil-fuel CO_2 emissions, although with a delay because emission adjustments are based on the warming and cumulative emissions since preindustrial. As a result, the 2°C target is reached later than in *2°C-ref* (Fig. 2c). In contrast, in the *2°C-r100-Eref* simulation, where freshwater forcing is terminated after 100 years and the AMOC gradually recovers, GSAT returns toward the reference

https://doi.org/10.5194/egusphere-2026-3065
Preprint. Discussion started: 24 June 2026

stabilization trajectory without emission adjustments, highlighting the tight coupling between AMOC strength and global temperature in this model.

Regionally, the AMOC collapse produces a characteristic bipolar temperature change pattern (Fig. 3c) (Stouffer et al., 2006; Vellinga and Wood, 2002; van Westen et al., 2024). The Northern Hemisphere cools substantially, with a hemispheric-mean anomaly of -1.51 °C (-1.69 to -1.30) during 2171–2200 relative to *2°C-ref*. This cooling is statistically significant across nearly the entire Northern Hemisphere. Even relative to preindustrial conditions the AMOC collapse produces a cooling in the North Atlantic region (Fig. 3b). The strongest annual-mean anomalies of up to -6.75 °C (-6.18 to -7.26) occur in the subpolar North Atlantic and extend zonally into Western and Central Europe (Fig. 3c). Over land, Europe and Asia cool by -2.27 °C (-2.71 to -1.98) and -1.70,°C (-1.93 to -1.45) respectively (Fig. B3). In contrast, the Southern Hemisphere exhibits a weaker and more heterogeneous response, with a small hemispheric-mean anomaly of -0.14 °C (-0.21 to -0.06). Land regions cool slightly, while parts of the mid-latitude oceans warm, although changes are not statistically significant everywhere. Consistent with the global evolution described above, a renewed strengthening of the cooling signal occurs toward the end of the simulation period (Fig. 2d), particularly over Europe (Fig. B3), as the AMOC remains in a persistently weak state.

The seasonal cycle of temperature changes over selected cities (e.g. Reykjavik, London, Bern, Beijing, Bergen) in the Northern Hemisphere reveals a pronounced winter amplification of the AMOC-induced cooling, especially in regions close to the North Atlantic (Fig. 3e,f). In the *2°C-ref* simulation, monthly temperatures averaged over 2171–2200 in all selected cities are above preindustrial levels throughout the year (Fig. 3d). In contrast, under AMOC collapse conditions (*2°C-hos-Eref*), the selected cities experience monthly mean temperatures at (Beijing) or below (Reykiavik, London, Bern, Bergen) preindustrial levels for much of the year (Fig. 3e). Temperature generally remains above -2 °C relative to 1861-1900 for most cities, except Reykjavik and London in winter. The largest cooling relative to *2°C-ref* is simulated in late winter and early spring (Fig. 3f). For example, Reykjavik cools by -6.77 °C (-9.70 to -4.14) in March relative to *2°C-ref*, while Bergen, London, and Vienna also exhibit strong winter cooling exceeding 3–4 °C. Cooling is substantially weaker in summer (Bellomo and Mehling, 2024; Jackson et al., 2015).

The temporal evolution of temperature changes also differs markedly among the selected cities. Reykjavik experiences the strongest and most rapid cooling following the onset of the AMOC collapse in 2026, with temperatures decreasing by -3.3 °C (-5.5 to -0.5) during 2031–2040 (Fig.B4). In contrast, cities farther inland, such as Bern, exhibit a more gradual decline in temperature extending until approximately 2060. Overall, the simulations indicate that cities located farther north and in closer proximity to the North Atlantic experience both stronger and more rapid cooling responses to AMOC collapse.

3.3 Drivers of global temperature response

AMOC changes strongly affect meridional ocean heat transport and regional climate. Previous studies showed that an AMOC weakening increases Arctic and North Atlantic sea-ice cover, enhancing global albedo, although the resulting impact on transient climate sensitivity was estimated to be modest (of the order of 10%; Swingedouw et al., 2006). Other modelling studies, however, have reported substantially larger global temperature responses to AMOC weakening or collapse (Drijfhout, 2015). In our simulations, the global mean surface air temperature difference of -0.83°C (-0.94 to -0.69°C) between *2°C-hos-Eref* and

https://doi.org/10.5194/egusphere-2026-3065
Preprint. Discussion started: 24 June 2026

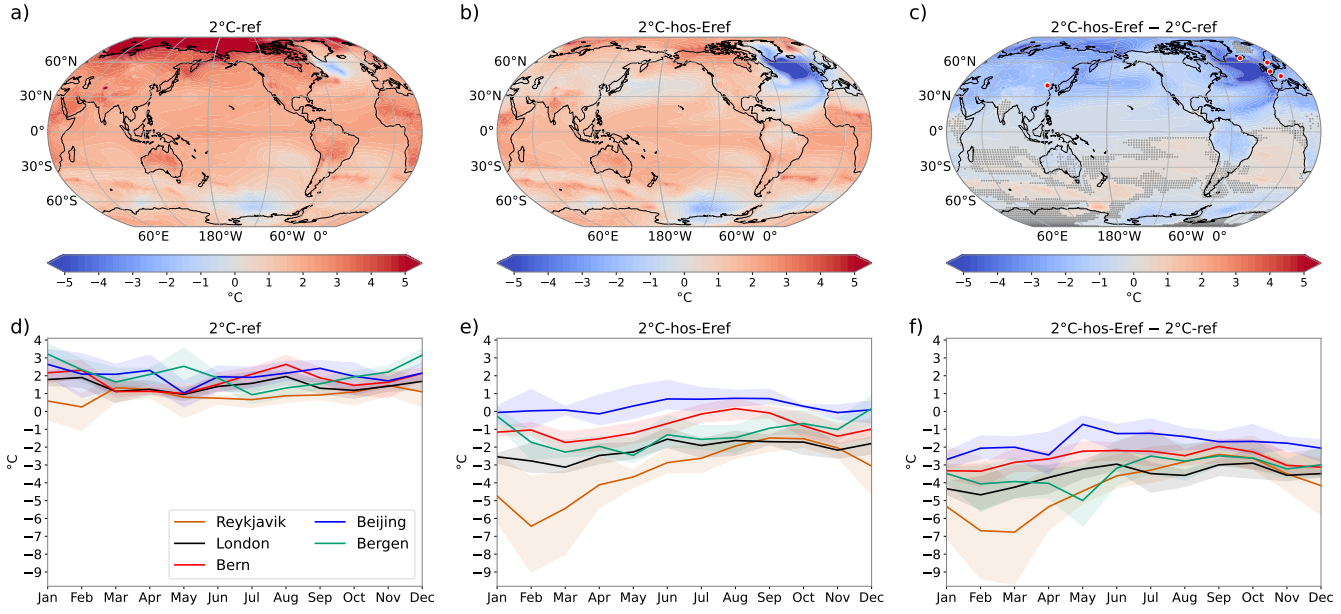

Figure 3. Regional surface air temperature response to an AMOC collapse. Mean surface air temperature in 2171-2200 for (a) *2°C-ref* relative to 1861-1900, (b) *2°C-hos-Eref* relative to 1861-1900, and (c) the difference between the two. Stippling in (c) marks regions where differences are not significant at the 5% level (two-sided t-test across ensemble members). Red dots in (c) indicate the locations of the cities shown in (d-f). Monthly mean surface air temperature in 2171-2200 for selected locations for (d) *2°C-ref* relative to 1861-1900, (e) *2°C-hos-Eref* relative to 1861-1900, and (f) the difference between the two. Shading indicates the ensemble range.

2°C-ref over 2171–2200 (Fig. 2d), corresponding to a 40% reduction in global warming, is very large. To better understand the GSAT response to AMOC collapse, we apply a climate feedback decomposition to quantify the contributions from cloud, ice-albedo, water-vapour, and carbon-cycle feedbacks (see Methods).

Changes in physical climate feedbacks dominate the global mean cooling of -0.83 °C (-0.93 to -0.69) over 2171–2200 following the AMOC collapse (Fig. 4a). Altered physical feedbacks account for 79 % (74 to 86) of the GSAT anomaly. Enhanced ocean heat uptake contributes 13 % (5 to 21), while the reduction in atmospheric CO_2 of 12.8 ppm (11.2 to 16.3; Section 3.5) explains a further 8 % (6 to 10) of the cooling.

Among individual components, cloud feedback changes dominate the cooling response (Fig. 4b) with an induced cooling of more than -0.5 °C. The AMOC collapse increases low-level cloud cover over the North Atlantic, enhancing cloud albedo and therefore shortwave reflection and inducing regional cooling (Fig. B5). Because the net cloud feedback in GFDL ESM2M is negative, the increased low-level cloud cover amplifies the global cooling relative to *2°C-ref*.

Changes in Planck, surface albedo, and combined water vapor–lapse rate feedbacks are relatively small. An exception occurs in the initial decades, when strongly increased surface albedo, driven by strongly expanding Northern Hemisphere sea ice (Fig. B6), contributes to the reduction in global temperature. After mid-century, sea ice declines slightly more in *2°C-hos-Eref*

https://doi.org/10.5194/egusphere-2026-3065
Preprint. Discussion started: 24 June 2026

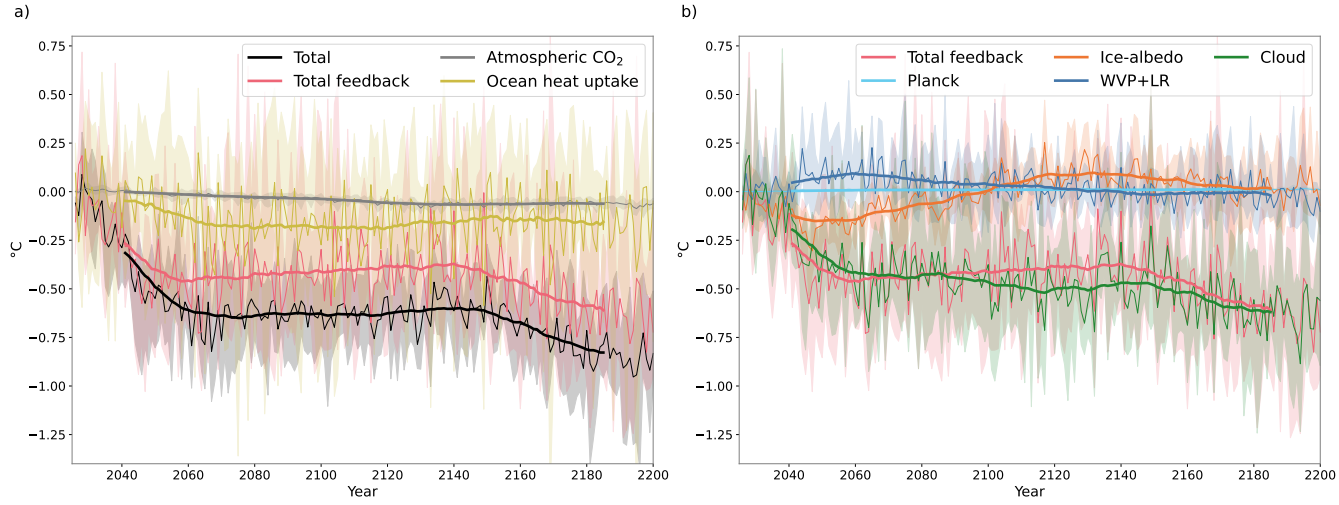

Figure 4. Contribution of individual drivers of the global mean surface air temperature change between *2°C-hos-Eref* and *2°C-ref* simulations. (a) Decomposition of GSAT changes into contributions from changes in feedbacks (λ), changes in ocean heat uptake (OHU), and changes in atmospheric CO_2 concentration. (b) Global mean surface air temperature change due to changes in individual feedbacks, such as Plank feedback, surface albedo feedback, water vapor and lapse rate feedbacks, and cloud feedback. Thicker lines in (a) and (b) represent a 31-year rolling mean. The lines represent the ensemble mean, and the shadings represent the ensemble spread.

than in *2°C-ref*. As a result, the ice-albedo driven cooling relative to *2°C-ref* declines and turns into a slight warming after 2100, indicating a smaller expansion of sea ice in *2°C-hos-Eref* after 2100 than what would be expected from the global cooling. By 2200, the effect of the change in ice-albedo feedback on the global mean cooling in *2°C-hos-Eref* is near zero.

Thus, cloud feedbacks are the primary driver of the global cooling following AMOC collapse in this model. The cooling is dominated by enhanced low-level cloud cover over the North Atlantic, which increases shortwave reflection and amplifies the regional cooling anomaly. This cloud response is consistent with enhanced lower-tropospheric stability over anomalously cold sea-surface temperatures, favoring the formation and persistence of low-level marine stratocumulus and stratus clouds.

3.4 Ocean heat and thermosteric sea level responses

The AMOC collapse strongly suppresses northward ocean heat transport, leading to a pronounced redistribution of heat between hemispheres (Fig. 5). Although the North Atlantic experiences a substantial decrease in ocean heat content, this regional cooling is more than offset by enhanced heat storage at lower latitudes and in the Southern Hemisphere (Fig. 5c). As a result, global ocean heat content (OHC) in *2°C-hos-Eref* is 488 ZJ (442 to 531 ZJ) higher than in *2°C-ref* during 2171–2200.

A zonally and depth-integrated heat budget shows the ocean north of 20°N loses 254 ZJ of heat content relative to *2°C-ref*. The reduction in northward ocean heat transport (-1562 ZJ) exceeds the concurrent reduction in ocean heat loss to the atmosphere (+1308 ZJ), resulting in a net decrease in regional heat storage. The positive cumulative surface heat flux anomaly north of 20°N primarily reflects reduced upward turbulent heat loss from the colder North Atlantic rather than enhanced

https://doi.org/10.5194/egusphere-2026-3065
Preprint. Discussion started: 24 June 2026

downward heat flux from the atmosphere (Fig. 5), consistent with the spatial pattern of cumulative surface heat flux anomalies (Fig. 5b).

In contrast, south of 20°N, excess heat accumulates in the tropics and Southern Hemisphere, consistent with diminished meridional heat redistribution. The net global OHC increase of 488 ZJ corresponds to 14% of the total ocean heat gain in *2°C-ref* relative to preindustrial conditions. This additional heat storage enhances thermosteric expansion and contributes to increased sea-level rise under AMOC collapse conditions.

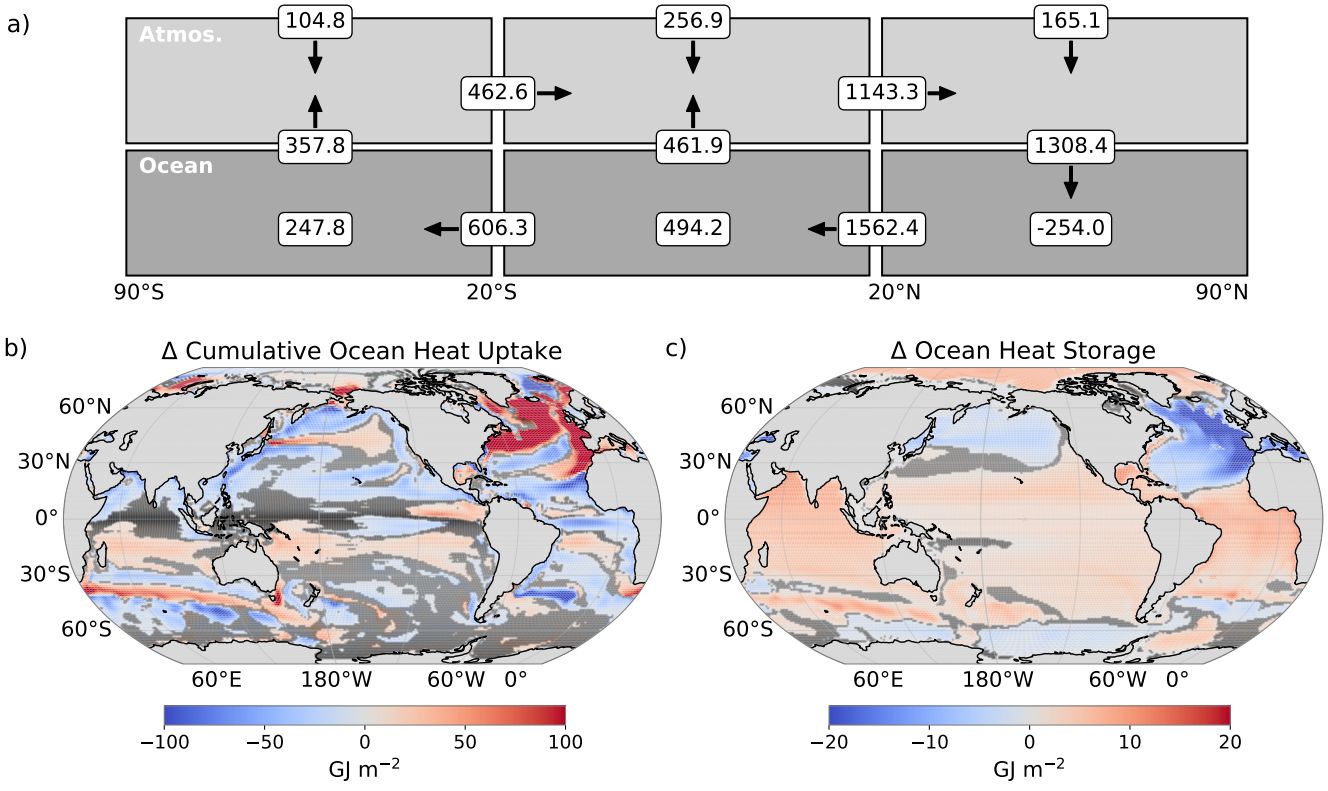

Figure 5. Earth system heat redistribution associated with AMOC collapse. (a) Difference in integrated heat fluxes and storage between *2°C-hos-Eref* and *2°C-ref*, averaged over 2171-2200 (in ZJ). Atmosphere heat transport is diagnosed as the residual between the net top-of-atmosphere radiative flux and the surface ocean heat flux. Ocean heat content (OHC) is calculated from temperature changes, and integrated ocean heat transport is derived as the residual of time-integrated surface heat flux and OHC. (b) Spatial distribution of cumulative ocean heat uptake from the atmosphere (time-integrated surface heat flux, in GJ m^{-2}). (c) Spatial distribution of ocean heat storage change between simulations (in GJ m^{-2}). Stippling in (b) and (c) marks regions where differences are not statistically significant at the 5% level (two-sided t-test across ensemble members).

Global thermosteric sea level rise reaches 28 cm (28 to 29 cm) by 2171–2200 in the *2°C-ref* simulation relative to preindustrial conditions. In *2°C-hos-Eref*, enhanced ocean heat uptake causes an additional 3 cm (3 to 4 cm) of thermosteric sea level

https://doi.org/10.5194/egusphere-2026-3065
Preprint. Discussion started: 24 June 2026

rise. Even after the hosing perturbation ceases (*2°C-r100-Eref*), thermosteric sea level remains elevated by 3 cm relative to *2°C-ref*, highlighting the long adjustment timescale and thermal memory of the ocean (Lacroix et al., 2024).

Regional thermosteric sea level differences between *2°C-ref* and *2°C-hos-Eref* exhibit pronounced spatial heterogeneity (Fig. 6b). The fastest and largest reductions occur along the eastern boundary of the North Atlantic. By 2171–2200, thermosteric sea level is lower by 115 cm (111 to 118 cm) in Casablanca (Morocco) and 78 cm (76 to 80 cm) in Lisbon (Portugal) relative to *2°C-ref* (Fig. 6c; Fig. B7). Smaller decreases, of up to 20 cm, also occur in parts of the North Pacific. In contrast, western boundary regions of the North Atlantic experience enhanced thermosteric sea level rise. For example, Miami shows an additional increase of 32 cm (30 to 34 cm).

Outside the North Atlantic, thermosteric sea level generally increases in the tropics and Southern Hemisphere under AMOC collapse. This response is particularly pronounced in the northern Indian Ocean, where thermosteric sea level rise increases by 18 cm (16 to 19 cm) in regions such as Karachi (Pakistan), and in the tropical Atlantic, where increases reach about 48 cm (45 to 51 cm) near Lagos (Nigeria). These regional increases are consistent with enhanced subsurface heat storage in these basins (Fig. 5c).

It should be noted that the thermosteric component presented here excludes dynamic sea level changes associated with AMOC weakening or collapse, which may further amplify sea level rise along the boundaries of the North Atlantic Ocean (Van Westen et al., 2026). Dynamic sea level changes are not included in the present analysis because the large and spatially localized freshwater forcing applied in the hosing experiments complicates physically meaningful separation of the additional volume effect from the purely dynamical effect, particularly in the North Atlantic (Fig. B8).

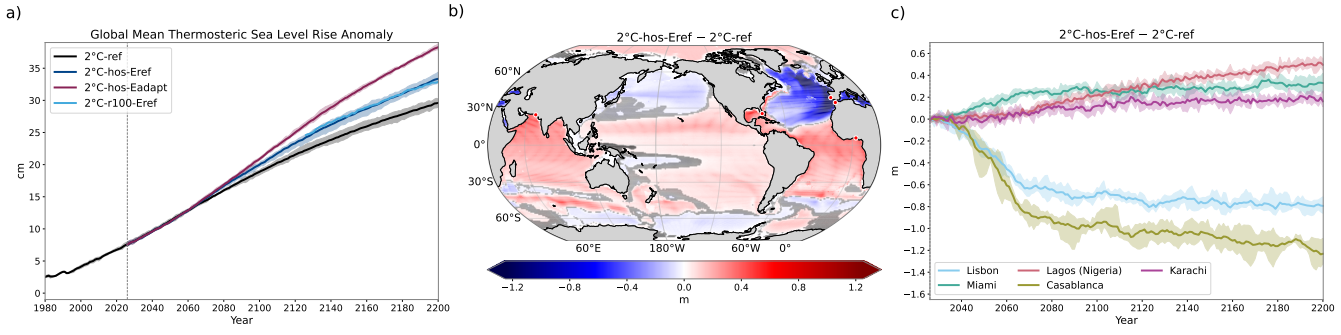

Figure 6. Thermosteric sea-level rise under different climate scenarios. (a) Global annual-mean, vertically integrated thermosteric sea-level rise in the hosing simulations *2°C-hos-Eref* and *2°C-hos-Eadapt*, the recovery simulation *2°C-r100-Eref*, and the reference simulation *2°C-ref*, relative to preindustrial conditions (1861–1900). (b) Spatial distribution of the thermosteric sea-level rise anomaly during 2170–2200, calculated as the difference between *2°C-hos-Eref* and *2°C-ref*. Red dots indicate locations shown in (c). (c) Differences in thermosteric sea-level rise between *2°C-hos-Eref* and *2°C-ref* for selected coastal cities. The vertical dashed line marks the beginning of the future scenario simulations in 2026.

https://doi.org/10.5194/egusphere-2026-3065
Preprint. Discussion started: 24 June 2026

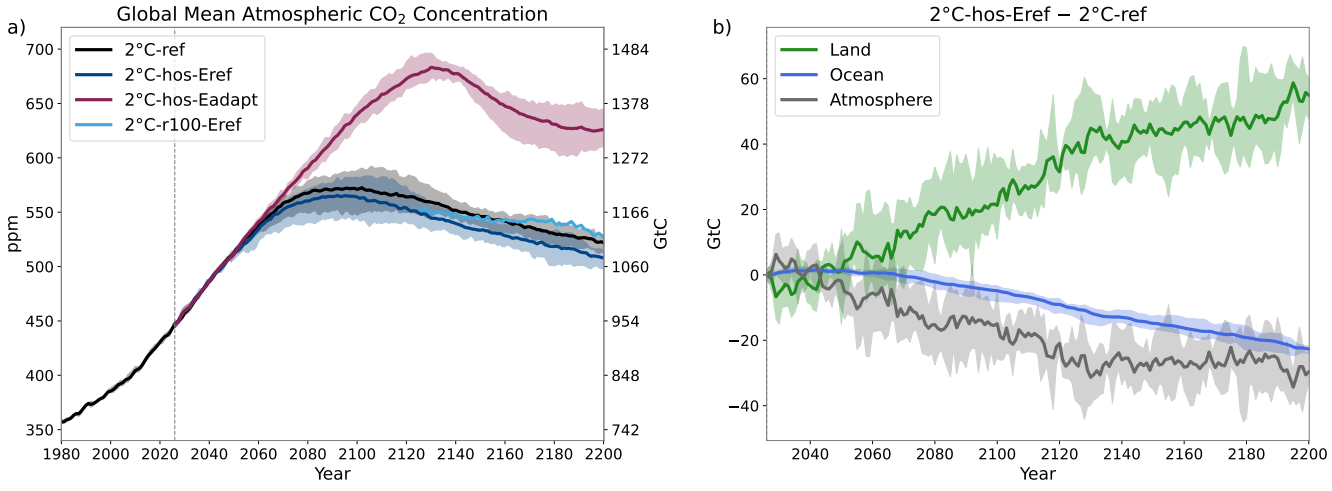

Figure 7. Atmospheric CO_2 and carbon inventory changes following an AMOC collapse. (a) Global annual mean atmospheric CO_2 concentrations for the hosing scenarios *2°C-hos-Eref* & *2°C-hos-Eadapt*, the recovery scenario *2°C-r100-Eref*, and the reference simulation *2°C-ref* without hosing. (b) Changes in integrated carbon inventories for the land, ocean, and atmosphere, shown as differences between *2°C-hos-Eref* and *2°C-ref*. The vertical dashed line marks the start year (2026) of the future scenario simulations.

3.5 Carbon cycle response

The AMOC collapse reduces atmospheric CO_2 by -12.8 ppm (-16.3 to -11.2), equivalent to -27.1 GtC (-34.5 to -23.8), by 2200 in *2°C-hos-Eref* relative to *2°C-ref* (Fig. 7a). Atmospheric CO_2 declines steadily relative to 2°C-ref until around 2120, after which the difference between the scenarios stabilizes (Fig. 7b). The atmospheric CO_2 response is primarily driven by enhanced land carbon uptake (+49.6 GtC; 44.5 to 59.9), partially offset by a reduction in ocean carbon storage (-14.3 GtC; -16.4 to -12.4; Fig. 7b).

Land-carbon changes exhibit a pronounced hemispheric asymmetry (Fig. 8a). In the Southern Hemisphere, land carbon storage increases by 63.9 GtC (56.3–74.0, 2171–2200), primarily driven by enhanced carbon uptake in the Amazon region, with smaller contributions from southern Africa and Australia. In these regions, increases in net primary production (NPP; (Fig. 8c)) outweigh opposing effects from elevated soil respiration and land-use and fire-related losses (Fig. 8b,d). These carbon gains coincide with wetter conditions (Fig. 8e, f), consistent with a southward shift of the Intertropical Convergence Zone (ITCZ), which, together with cooler global temperatures, promotes vegetation productivity and soil carbon accumulation.

In contrast, the Northern Hemisphere exhibits a net carbon loss of -13.7 GtC (-19.72 to -5.7), driven by widespread declines in NPP that exceed reductions in soil respiration, fire emissions, and land-use losses. Colder and drier conditions across northern Africa, Europe, and Asia suppress NPP more strongly than soil respiration, leading to net carbon losses. Exceptions are northern North America, northern Europe and Siberia, where reductions in soil respiration outweigh declines in NPP, leading to a regional net carbon gain.

https://doi.org/10.5194/egusphere-2026-3065
Preprint. Discussion started: 24 June 2026

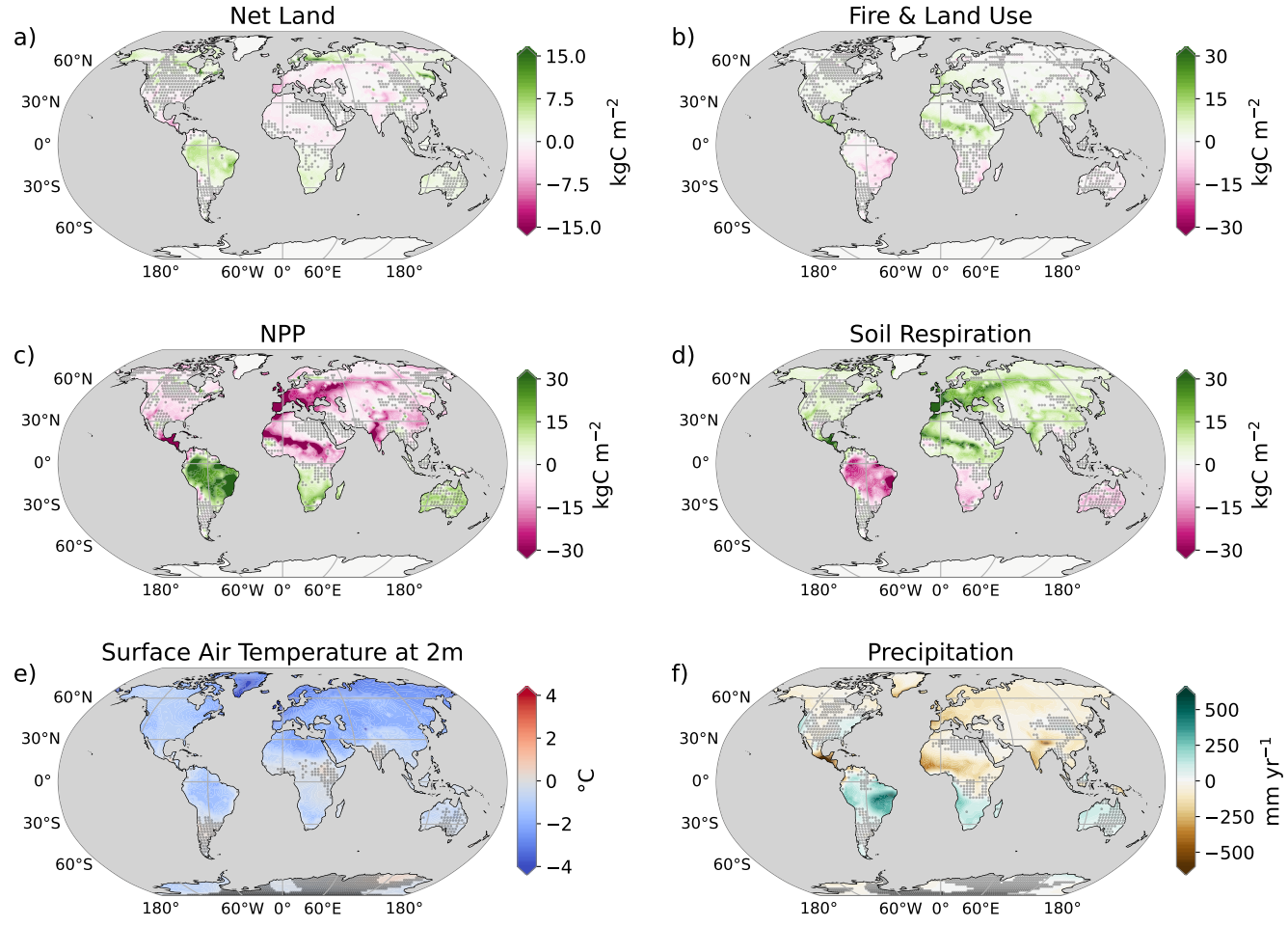

Figure 8. Spatial distribution of cumulative (time-integrated) land carbon flux responses to an AMOC collapse. Shown are differences between the *2°C-hos-Eref* and *2°C-ref* simulations for 2171-2200 in (a) net land carbon flux, (b) carbon losses from fire and land use change, (c) net primary production (NPP), (d) soil respiration, (e) surface air temperature, and (f) precipitation. Positive values in (a)–(d) indicate carbon fluxes from the atmosphere to the land (e.g. increased soil respiration yields negative values in panel d). Stippling indicates regions where differences are not statistically significant at a 5% level (Welch's t-test).

Similar to the pronounced hemispheric redistribution of ocean heat uptake and storage, the AMOC collapse also reorganizes ocean carbon uptake and storage (Fig. 9). Reduced northward carbon transport (-33 GtC) leads to a widespread decline in ocean carbon inventory across most of the Northern Hemisphere, with the largest decreases in carbon storage per area in the North Atlantic. South of 20°N, CO_2 outgasses to the atmosphere in many regions, reflecting the lower atmospheric CO_2 concentrations driven by enhanced land carbon uptake, and amplified by reduced northward transport of dissolved inorganic carbon. Despite this overall outgassing, ocean carbon uptake north of 20°N is slightly enhanced in the collapse case, reflecting compensating spatial patterns: reduced uptake along the eastern North Atlantic boundary is offset by increased uptake along the

https://doi.org/10.5194/egusphere-2026-3065
Preprint. Discussion started: 24 June 2026

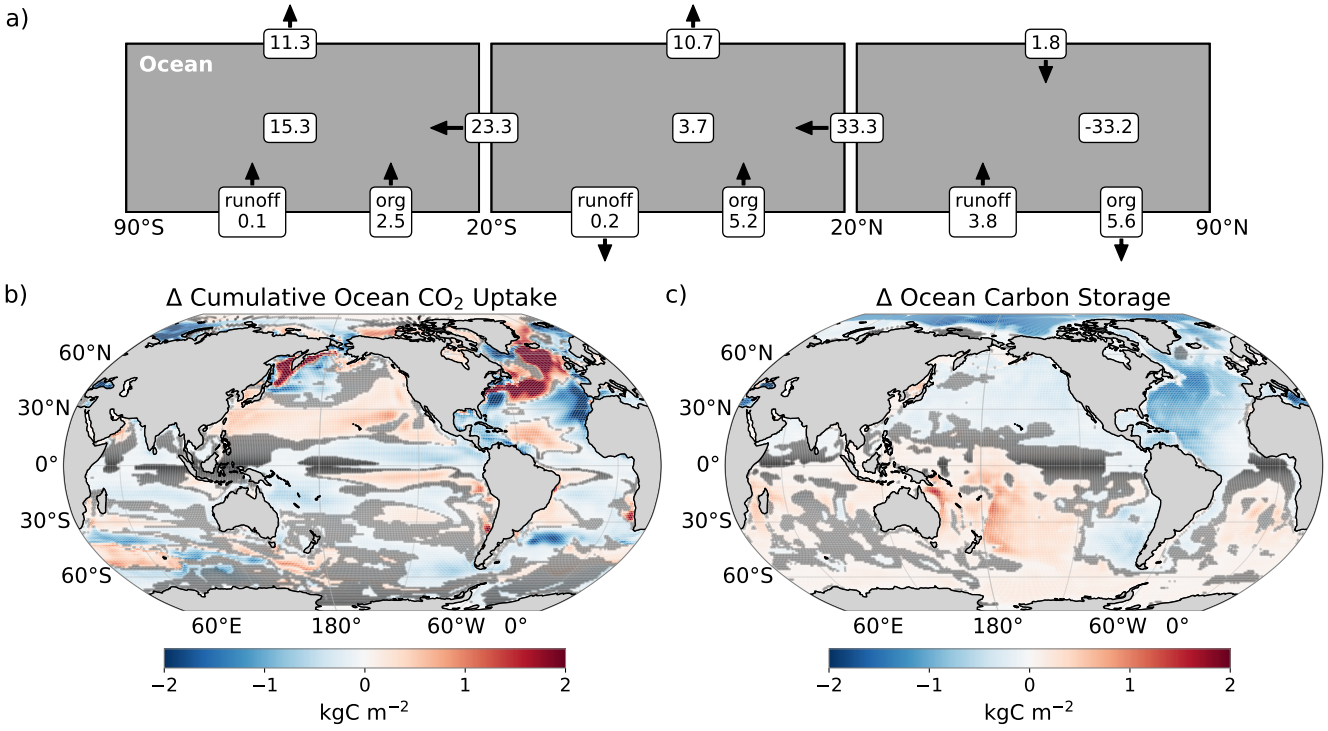

Figure 9. Cumulative (time-integrated) ocean carbon flux and storage responses to an AMOC collapse. (a) Integrated changes in carbon fluxes and storage between between the *2°C-hos-Eref* and *2°C-ref* simulations for 2171–2200 in GtC. *runoff* represents DIC input from rivers, and *org* represents the carbon exchange with organic carbon reservoirs, including ocean sediments. Transport terms at 20°N and 20°S indicate residuals from the north and tropic regions. (b) Spatial distribution of changes in cumulative ocean carbon uptake. (c) Spatial distribution of the vertically integrated carbon storage changes. Dots in (b) and (c) indicate regions where differences are not statistically significant at the 5% level (Welch's t-test).

western boundary and south of Iceland. Changes in riverine carbon input and internal sources and sinks of dissolved inorganic carbon associated with shifts in organic matter production and sediment carbon fluxes are relatively small.

3.6 Implications for the transient climate response to cumulative emissions and the remaining emission budget

Changes in global mean temperature and atmospheric CO_2 associated with the AMOC collapse have important implications for the linearity of the transient climate response to cumulative emissions (TCRE; Allen et al. (2009)) and the remaining emission budget (Matthews et al., 2020). In the *2°C-hos-Eref* experiment, the collapse interrupts the near-linear relationship between global warming and cumulative emissions: despite following identical CO_2 emission pathways and cumulative totals as in *2°C-ref* (Fig. 10a), global warming is effectively stalled. This decoupling of warming from cumulative emissions leads to a departure from the canonical TCRE linearity (Fig. 10b).

https://doi.org/10.5194/egusphere-2026-3065
Preprint. Discussion started: 24 June 2026

To quantify the implications for the remaining emission budget, we analyse the *2°C-hos-Eadapt* scenario, in which CO_2 emissions are increased in order to still achieve 2°C warming under a collapsed AMOC (Fig. 10a). In this case, cumulative CO_2-forcing-equivalent emissions increase by 437 GtC (379–507) by year 2200 relative to *2°C-ref*, corresponding to a 24% (20–28) increase in the total carbon budget since preindustrial time (Fig. 10b). When considering only emissions after 2026, the remaining emission budget increases by 60% (49–73).

Following the initial disruption caused by the AMOC collapse, the *2°C-hos-Eadapt* simulation re-establishes an approximately linear relationship between cumulative emissions and global warming as emissions continue. For cumulative emissions between year 2051 and 2150, the slope in *2°C-ref* is 1.00 °C (0.65 to 1.40) per 1000 GtC, which is slightly smaller than the corresponding slope in *2°C-hos-Eref* of 1.25 (1.03 to 1.52) °C per 1000 GtC obtained over the period 2046 to 2140.

Finally, in the *2°C-r100-Eref* scenario where the AMOC recovers when the freshwater hosing is stopped, the remaining emission budget returns to levels comparable to the *2°C-ref* simulation. This result demonstrates that the suppressed TCRE and enhanced remaining emission budget under AMOC collapse are reversible in our model framework: once the AMOC is restored to the strength of the non-hosing reference simulation, the standard linear relationship between global warming and cumulative CO_2 emissions is recovered.

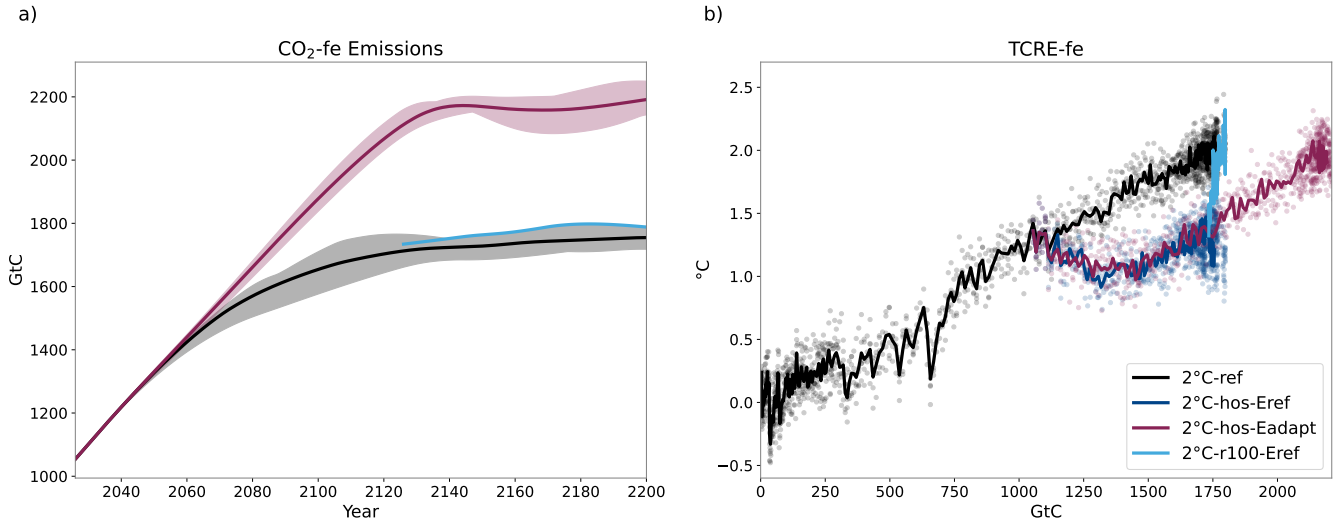

Figure 10. Cumulative CO_2-fe emissions and TCRE-fe. (a) Cumulative CO_2 forcing equivalent (CO_2-fe) emissions in GtC and (b) TCRE-fe of the hosing scenarios *2°C-hos-Eref* & *2°C-hos-Eadapt* , the recovery scenario *2°C-r100-Eref*, and the *2°C-ref* simulation. The solid lines show the ensemble mean, the shadings represent the ensemble spread, and the circles represent the individual ensemble members. CO_2-fe emissions for all non-CO_2 agents represent the CO_2 emissions that would produce the same radiative forcing trajectory as these non-CO_2 emissions (Allen et al., 2018).

https://doi.org/10.5194/egusphere-2026-3065
Preprint. Discussion started: 24 June 2026

3.7 Sensitivity to background temperature levels

Comparing the hosing and no-hosing experiments under preindustrial and transient 2°C global warming background states reveals a systematically weaker AMOC response in the warmer climate. At 26.5°N, the freshwater-induced AMOC weakening is 16% (12 to 22) smaller under 2°C warming than under preindustrial conditions (Table 2; Fig. B1), with comparable reductions also found at 48°N (not shown). The associated climate responses are likewise attenuated in the warmer background state (Table 2). In particular, GSAT cooling is 38% (18 to 50) weaker, winter cooling over Reykjavik is reduced by 58% (31 to 84), the global ocean heat content anomaly is 30% (12 to 42) smaller, and global thermosteric sea level rise decreases by 26% (12 to 42). Overall, these results indicate a reduced sensitivity of the climate system to AMOC collapse under warmer background conditions. This suggests that climate impacts inferred from preindustrial hosing experiments (van Westen et al., 2024) may overestimate the magnitude of future AMOC-collapse responses in a greenhouse-warmed world. The weaker response likely reflects changes in the mean state of the coupled climate system under warming, including altered ocean stratification, sea-ice extent, and air–sea heat exchange, although a detailed process-based attribution is beyond the scope of this study. A notable exception is atmospheric CO_2, which exhibits a 40% (15 to 90) larger decrease under 2°C warming than under preindustrial conditions. This enhanced CO_2 response points to potentially different sensitivities of ocean and terrestrial carbon uptake and storage processes under warmer climate states, despite the generally weaker physical climate response to AMOC collapse.

Variable	Preindustrial	+2°C	Ratio (+2°C / preindustrial)
AMOC at 26.5°N (Sv)	-17.2 (-17.8 to -16.6)	-14.4 (-14.6 to -13.8)	0.84 (0.78 to 0.88)
Global annual mean 2-m air temperature (°C)	-1.3 (-1.4 to -1.1)	-0.8 (-0.9 to -0.7)	0.62 (0.50 to 0.82)
Winter (DJF) 2-m air temperature in Reykjavik (°C)	-13.0 (-15.9 to -10.4)	-5.4 (-7.2 to -2.5)	0.42 (0.16 to 0.69)
Global ocean heat content (ZJ)	699 (635 to 765)	488 (442 to 531)	0.70 (0.58 to 0.84)
Global thermosteric sea level rise (cm)	4.6 (4.2 to 5.0)	3.4 (2.9 to 3.7)	0.74 (0.58 to 0.88)
Global atmospheric CO_2 concentration (ppm)	-9.2 (-9.7 to -8.6)	-12.8 (-16.3 to -11.2)	1.39 (1.15 to 1.90)

Table 2. Dependence of climate system responses to a 0.3 Sv uniform freshwater hosing under different background climate states. Values show ensemble mean anomalies after 146-175 years of starting hosing, with the ensemble spread in brackets. 'Future' refers to anomalies in *2°C-hos-Eref* relative to *2°C-ref*, while 'Preindustrial' refers to anomalies in *piControl-hos* relative to a preindustrial control simulation. 'Ratio' denotes the ratio of the future to preindustrial anomalies.

.

4 Discussion and Conclusions

This study examines how a potential AMOC collapse would affect the physical climate system and carbon cycle under pathways that limit global warming to 2 °C. A collapse of the AMOC produces pronounced global and regional temperature anomalies, including strong cooling across northern Europe, and drives large-scale redistributions of ocean heat and carbon.

https://doi.org/10.5194/egusphere-2026-3065
Preprint. Discussion started: 24 June 2026

These changes reduce atmospheric CO_2 concentration through enhanced land carbon uptake, which is most pronounced in tropical South America. Although the collapse-induced cooling temporarily disrupts the TCRE-fe relationship and increases the remaining emissions budget, these effects occur alongside severe regional climate impacts.

Our simulations show a substantial global cooling of up to 0.8°C due to the AMOC collapse. Previous studies using the same model family (Winton et al., 2013) demonstrated that an AMOC slowdown redistributes ocean heat uptake from subtropical surface regions to higher latitudes, a pattern that is also evident in our simulations (Fig. 5). Because the climate system is particularly sensitive to high-latitude forcing (Winton et al., 2010; Rugenstein et al., 2013; Gregory et al., 2024), this shift leads to a disproportionately large reduction in global mean surface air temperature, thereby suppressing surface warming (Winton et al., 2013). This behavior is consistent with the pattern-dependent climate-feedback framework, in which feedback strength depends on the spatial pattern of surface temperature change and ocean heat uptake (Winton et al., 2010; Armour et al., 2013; Rose et al., 2014). In our simulations, the reduction of ocean heat transport to the high-latitude North Atlantic, combined with enhanced high-latitude heat uptake, strengthens negative cloud feedbacks (Fig. B5), further amplifying the cooling. These results are consistent with earlier studies showing that models with a pronounced AMOC weakening tend to exhibit slower historical warming rates (Bonnet et al., 2021). They also align with the findings of Drijfhout (2015), who reported a global cooling effect associated with an AMOC weakening and with Trossman et al. (2016), who showed that AMOC weakening helps maintain low cloud cover in the face of global warming. The simulated increase in total ocean heat content due to AMOC collapse is consistent with paleoclimate reconstructions and model studies, which indicate enhanced top-of-atmosphere energy imbalance and increased ocean heat storage during periods of strongly reduced AMOC strength (Baggenstos et al., 2019; Katsman and van Oldenborgh, 2011; Pedro et al., 2018; Galbraith et al., 2016).

Our simulations indicate that atmospheric CO_2 decreases under an AMOC collapse relative to the non-collapse experiment, primarily due to enhanced terrestrial carbon uptake. This outcome contrasts with Boot et al. (2024), who find a small increase in atmospheric CO_2 following an AMOC shutdown, driven mainly by ocean outgassing. Although the magnitude of the atmospheric CO_2 response is modest in both studies (-13 ppm here vs. +4 ppm under SSP5-8.5 scenario in Boot et al. (2024)), the opposite signs are consistent with previous multi-model assessments showing large inter-model uncertainty in the carbon-cycle response to AMOC weakening, including disagreement on the direction of change as well as dependence on the background climate state (Gottschalk et al., 2019). These divergent responses highlight that the sign and magnitude of the atmospheric CO_2 perturbation are sensitive to model-specific representations of ocean circulation and carbon–climate feedbacks (Zickfeld et al., 2008). A coordinated model intercomparison analysis using harmonized forcing and experimental design will therefore be essential to identify the processes responsible for these differences and to assess the robustness of the carbon-cycle response to an AMOC collapse (Swingedouw et al., 2026).

Our results indicate that an AMOC collapse substantially alters the hydroclimate and carbon cycle of the tropical land regions, leading to increased land carbon uptake that dominates the global land-carbon response. The AMOC collapse induces a southward shift of the ITCZ, producing cooler and wetter conditions over the southern Amazon region that favor enhanced carbon storage. This response is broadly consistent with paleo-evidence from Heinrich Stadial 1, when an AMOC shutdown shifted the ITCZ southward and increased precipitation over southern tropical South America (Mulitza et al., 2017; Song and

https://doi.org/10.5194/egusphere-2026-3065
Preprint. Discussion started: 24 June 2026

Zhang, 2017; Campos et al., 2019). Correspondingly, paleo records link these wetter conditions to increased tree cover in southern Amazonia (Dupont et al., 2010; Nian et al., 2023), in line with the enhanced carbon uptake simulated herein. Our findings also agree with previous modelling studies showing that an AMOC tipping transition tends to increase rainfall in the southern Amazon and northeastern Brazil, potentially stabilizing parts of the rainforest (Ben-Yami et al., 2024; Ciemer et al., 2021; Nian et al., 2023; Wunderling et al., 2024). However, some of those modeling studies also show a drying of the northern Amazon due to an AMOC collapse, a feature not simulated in our model. In addition, future land-use change may also strongly influence forest resilience. Our simulations follow the RCP2.6 scenario where agricultural area does not further expand, which should be considered when interpreting the results.

Our results show that an AMOC collapse disrupts the near-linear relationship between global warming and cumulative CO_2 emissions (TCRE), as the AMOC-induced cooling temporarily decouples temperature from emissions during the tipping transition. Numerous studies have demonstrated that the TCRE provides a robust predictor of CO_2-driven warming under a wide range of forcing scenarios (Matthews et al., 2009; Allen et al., 2009; Tokarska et al., 2016; Matthews et al., 2020). Our findings suggest, however, that this near-linear relationship breaks down when the AMOC collapses, because the associated cooling offsets the warming expected from cumulative emissions. Once emissions continue under the collapsed-AMOC scenario, however, the relationship between global warming and cumulative emissions returns to an approximately linear trajectory, similar to that in the simulation without AMOC collapse (*2°C-ref*). Nevertheless, the TCRE slope remains slightly smaller in the collapsed-AMOC state, suggesting that AMOC-induced changes in ocean circulation modify to some extent the partitioning of heat and carbon uptake by the global ocean, thereby altering the transient warming response to cumulative CO_2 emissions in this model.

Most previous AMOC-collapse experiments with comprehensive Earth system models have imposed freshwater hosing under preindustrial climate conditions (Vellinga and Wood, 2002; Menviel et al., 2008; Bozbiyik et al., 2011; Jackson et al., 2015; Orihuela-Pinto et al., 2022; van Westen et al., 2024; Ma et al., 2024; Jackson et al., 2023), whereas here we investigate an AMOC collapse superimposed on a transient warming trajectory toward 2°C global warming. We find that, with the exception of atmospheric CO_2, the overall climate response to an AMOC collapse is generally weaker in the warming-world simulations than under preindustrial conditions. In particular, the cooling over the North Atlantic region and globally as well as the associated global ocean heat content changes are reduced relative to comparable preindustrial hosing experiments. This result is broadly consistent with the recent study by Bellomo and Mehling (2024), who also reported attenuated surface temperature and precipitation responses to AMOC weakening under greenhouse-warmed climate states. Together, these findings suggest that the background climate state can substantially modulate the magnitude of AMOC-collapse impacts, potentially through changes in ocean stratification, sea-ice feedbacks and cloud responses. A detailed attribution of the mechanisms responsible for these differences, however, lies beyond the scope of the present study. The forthcoming multi-model TIPMIP-ESM (Jones et al., 2025) and TIPMIP-OCEAN (Swingedouw et al., 2026) simulations will provide a broader framework for assessing the robustness and generality of these results across models and experimental designs.

Several limitations of our experimental design should be considered when interpreting the results. These include the use of idealized freshwater forcing, reliance on a single Earth system model with associated structural uncertainties, and relatively

https://doi.org/10.5194/egusphere-2026-3065
Preprint. Discussion started: 24 June 2026

short simulations that do not allow the climate system to fully equilibrate. First, the imposed freshwater forcing is spatially uniform, temporally constant, and unrealistically large, following the NAHosMIP protocol. In reality, freshwater input from ice melt is spatially heterogeneous, seasonally varying, and likely smaller in magnitude. Consequently, more realistic forcing would likely produce a weaker AMOC response and reduced climate and carbon cycle impacts. In addition, the strong freshwater perturbation and associated salinity changes affect surface biogeochemistry by diluting alkalinity and dissolved inorganic carbon (DIC), which may lead to an overestimation of the reduction in oceanic pCO_2 and thus carbon uptake in the North Atlantic (Boot et al., 2024). Local salinity decreases of up to 3–4 psu also reduce CO_2 solubility by 2–3%, partially offsetting the temperature-driven increase of up to 20%. Second, the GFDL ESM2M does not explicitly resolve mesoscale eddies and lacks interactive ice sheet components for Greenland and Antarctica, which may influence ocean circulation and AMOC variability. Third, our results are also based on a single model, and multi-model ensembles are required to assess the robustness of the simulated climate and carbon cycle responses. Finally, the hosing simulations do not reach equilibrium. Global cooling, for example, continues at the end of the simulations, indicating that longer integrations are needed to fully capture the equilibrated climate response.

In summary, our results indicate that a potential future AMOC collapse could profoundly reshape the climate and carbon cycle, with far-reaching implications for ecosystems and societies. While the associated cooling would temporarily ease global temperature targets and lower atmospheric CO_2, it would coincide with severe regional climate disruptions, particularly in Europe and the tropics, as well as substantial shifts in ocean and land carbon storage. These findings underscore the importance of accounting for AMOC stability in long-term climate risk assessments and highlight the need for coordinated multi-model efforts to better constrain the likelihood and impacts of an AMOC collapse.

Code and data availability. Observational data from the RAPID-MOCHA-WBTS array at 26°N is available under https://www.bodc.ac.uk/data/published_data_library/catalogue/10.5285/33826d6e-801c-b0a7-e063-7086abc0b9db/. The code used for this study and the analyzed simulation data will be made available at a later stage of the review.

Appendix A: Temperature Decomposition

To estimate the temperature response to an AMOC collapse, we use a simple energy balance model (Gregory et al., 2004):

$$\Delta T = \frac{\Delta F - \Delta N}{\Lambda}, \tag{A1}$$

where ΔT denotes the global mean surface air temperature anomaly, ΔF the radiative forcing, ΔN the net top-of-atmosphere radiation imbalance, and Λ the climate feedback parameter, all defined relative to preindustrial conditions. Within this framework, the climate feedback parameter Λ can be interpreted as the sum of contributions from different physical processes governing the temperature response to a radiative perturbation. We can decompose Λ into albedo feedback (λ_A), cloud feedback (λ_C), Planck feedback (λ_P) and a residual including the water vapor and lapse rate feedbacks (λ_W):

https://doi.org/10.5194/egusphere-2026-3065
Preprint. Discussion started: 24 June 2026

$$
\begin{aligned}
\Lambda &= \frac{\Delta F - \Delta N}{\Delta T} = \frac{\Delta F - \Delta N + \Delta N_0 - \Delta N_0}{\Delta T} \quad \text{(where } \Delta N_0 = \Delta SW_0 - \Delta LW_0\text{)} \\
&= -\frac{\Delta SW_0}{\Delta T} - \frac{\Delta N - \Delta N_0}{\Delta T} - \frac{-\Delta F - \Delta LW_0}{\Delta T} \\
&= -\frac{\Delta SW_0}{\Delta T} - \frac{\Delta N - \Delta N_0}{\Delta T} + \frac{d(\sigma T_e^4)}{dT} - \frac{\frac{d(\sigma T_e^4)}{dT}\Delta T - \Delta F - \Delta LW_0}{\Delta T} \\
&= \underbrace{-\frac{\Delta SW_0}{\Delta T}}_{\lambda_A} \underbrace{-\frac{\Delta N - \Delta N_0}{\Delta T}}_{\lambda_C} \underbrace{-\left(-4\sigma T_e^3\right)}_{\lambda_P} \underbrace{-\frac{4\sigma T_e^3 \Delta T - \Delta F - \Delta LW_0}{\Delta T}}_{\lambda_W} \\
&= -\lambda_A - \lambda_C - \lambda_P - \lambda_W
\end{aligned} \tag{A2}
$$

ΔF represents the change in radiative forcing from CO_2 (the only forcing agent that changes between the *2°C-hos-Eref* and *2°C-ref* simulation), ΔN is the change in net radiation at the top of the atmosphere (TOA), ΔT is the global surface air temperature anomaly, ΔN_0 is the clear-sky net radiation at TOA, ΔSW_0 and ΔLW_0 are the clear-sky net shortwave and longwave radiation at TOA, respectively, and T_e is the effective emission temperature. T_e is derived from the outgoing longwave radiation and the Stefan-Boltzmann law, $T_e = (LW/\sigma)^{1/4}$.

For ease of reading, we write the following $T = \Delta T$, $F = \Delta F$, $N = \Delta N$. We denote variables from hosing experiments (e.g., *2°C-hos-Eref*) by superscript h, and those from the reference simulation (*2°C-ref*) by ref. Differences between those two simulations for a given variable X are expressed as $\delta X = X^h - X^{ref}$.

We now decompose the change in temperature between the hosing and reference simulations δT as a function of changes in forcing (δF), ocean heat uptake (δN), and feedback changes ($\delta \Lambda$):

$$
\begin{aligned}
\delta T &= T^h - T^{ref} \\
&= \frac{F^h - N^h}{\Lambda^h} - \frac{F^{ref} - N^{ref}}{\Lambda^{ref}} \\
&= \frac{1}{\Lambda^h \Lambda^{ref}}[\Lambda^{ref}(F^h - N^h) - \Lambda^h(F^{ref} - N^{ref})] \\
&= \frac{1}{\Lambda^h \Lambda^{ref}}[\Lambda^{ref} F^h - \Lambda^{ref} N^h - \Lambda^h F^{ref} + \Lambda^h N^{ref}] \\
&= \frac{1}{\Lambda^h \Lambda^{ref}}[\Lambda^{ref}\delta F + \Lambda^{ref} F^{ref} - \Lambda^{ref}\delta N - \Lambda^{ref} N^{ref} - \Lambda^h F^{ref} + \Lambda^h N^{ref}] \\
&= \frac{1}{\Lambda^h \Lambda^{ref}}[\Lambda^{ref}\delta F - \Lambda^{ref}\delta N - F^{ref}\delta\Lambda + N^{ref}\delta\Lambda] \\
&= \frac{1}{\Lambda^h \Lambda^{ref}}[\Lambda^{ref}\delta F - \Lambda^{ref}\delta N - \underbrace{\left(F^{ref} - N^{ref}\right)}_{\Lambda^{ref} T^{ref}}\delta\Lambda] \\
&= \frac{1}{\Lambda^h}[\delta F - \delta N - T^{ref}\delta\Lambda] \\
&= \frac{\delta F}{\Lambda^{ref} + \delta\Lambda} - \frac{\delta N}{\Lambda^{ref} + \delta\Lambda} - \frac{T^{ref}\delta\Lambda}{\Lambda^{ref} + \delta\Lambda}
\end{aligned} \tag{A3}
$$

https://doi.org/10.5194/egusphere-2026-3065
Preprint. Discussion started: 24 June 2026

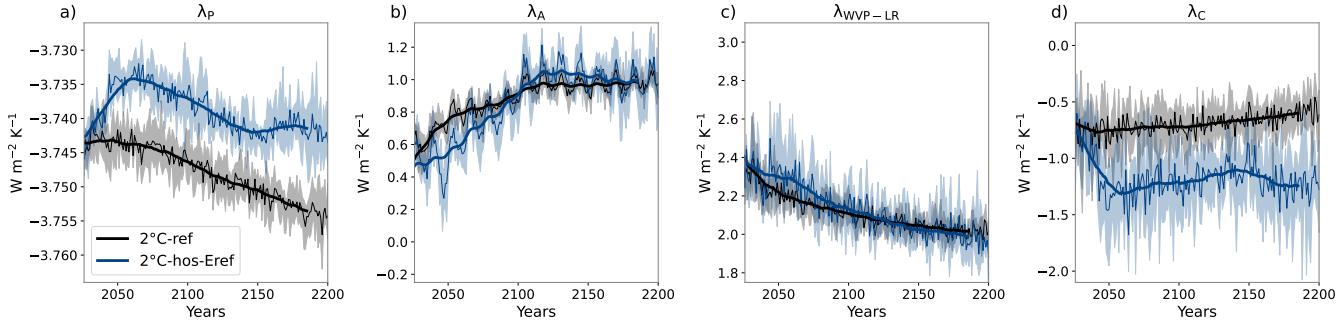

Figure A1. Feedback parameter decomposition for both *2°C-ref* and *2°C-hos-Eref* simulations. Λ is decomposed into (a) the Planck feedback λ_P, (b) the albedo feedback λ_A, (c) the water vapor and lapse rate feedback λ_W, and (d) the cloud feedback λ_C.

The three terms can be interpreted as the contributions from changes in radiative forcing, ocean heat uptake, and feedbacks, respectively, to the change in global temperature due to the hosing. All three terms are identically rescaled by changes in the feedback parameter between reference and hosing, $\delta\Lambda$, reflecting that the temperature response to a change in forcing or ocean heat uptake changes when climate feedbacks change at the same time. Notably, this nonlinear entanglement of forcing and heat uptake changes with feedback changes resolves for the relative contributions to the temperature change, such that the relative contribution from forcing and ocean heat uptake changes to temperature changes does not depend on feedback changes.

Following the decomposition of Λ in Eq. (A2), the feedback difference between the hosing and reference simulation decomposes as:

$$\delta\Lambda = -\delta\lambda_P - \delta\lambda_A - \delta\lambda_W - \delta\lambda_C, \tag{A4}$$

with $\delta\lambda_P$ the Planck feedback difference, $\delta\lambda_A$ the albedo feedback difference, $\delta\lambda_{WVP-LR}$ the residual including water vapor and lapse rate feedback difference, and λ_C the cloud feedback difference. This leads to a temperature decomposition consisting of six different terms

$$\delta T = \frac{T^{ref}}{\Lambda^{ref}+\delta\Lambda}(\delta\lambda_P + \delta\lambda_A + \delta\lambda_W + \delta\lambda_C) + \frac{\delta F}{\Lambda^{ref}+\delta\Lambda} - \frac{\delta N}{\Lambda^{ref}+\delta\Lambda}, \tag{A5}$$

where we define:

$$\left\{\begin{array}{l} \left.\begin{array}{l} \delta T_P = \dfrac{T^{ref}}{\Lambda^{ref}+\delta\Lambda}\delta\lambda_P \\ \delta T_A = \dfrac{T^{ref}}{\Lambda^{ref}+\delta\Lambda}\delta\lambda_A \\ \delta T_W = \dfrac{T^{ref}}{\Lambda^{ref}+\delta\Lambda}\delta\lambda_W \\ \delta T_C = \dfrac{T^{ref}}{\Lambda^{ref}+\delta\Lambda}\delta\lambda_C \end{array}\right\} \Rightarrow \text{changes in T due to changes in physical feedbacks} \\ \left.\begin{array}{l} \delta T_F = \dfrac{\delta F}{\Lambda^{ref}+\delta\Lambda} \end{array}\right\} \Rightarrow \text{change in T due to atmospheric CO2} \\ \left.\begin{array}{l} \delta T_N = -\dfrac{\delta N}{\Lambda^{ref}+\delta\Lambda} \end{array}\right\} \Rightarrow \text{change in T due to ocean heat uptake} \end{array}\right. \tag{A6}$$

https://doi.org/10.5194/egusphere-2026-3065
Preprint. Discussion started: 24 June 2026

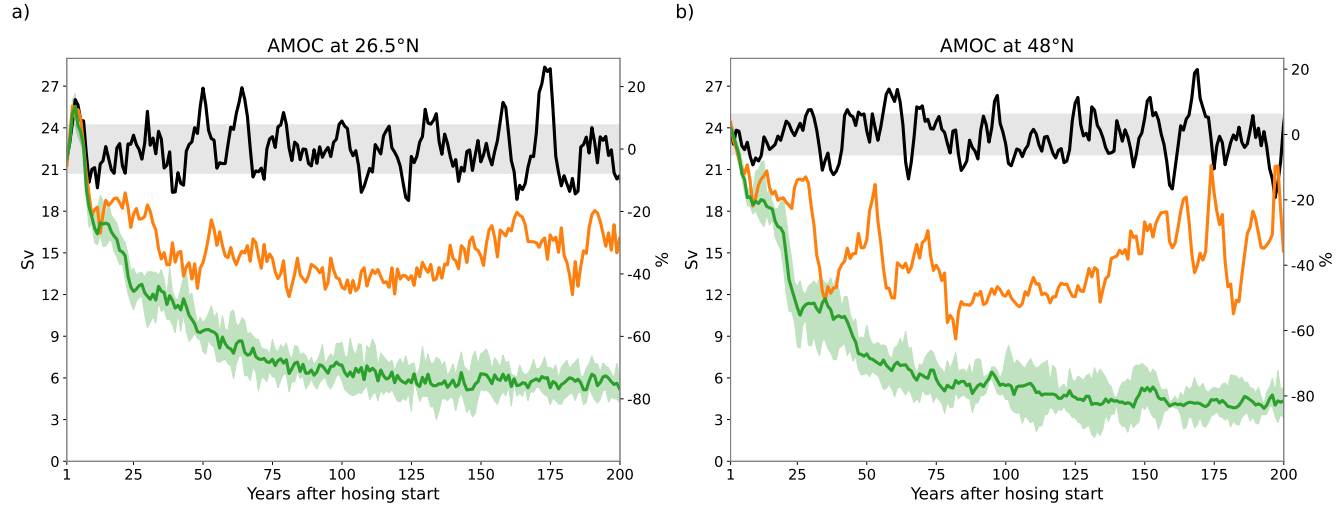

Figure B1. Annual mean AMOC strength at 26.5°N (a) and 48°N (b) in the preindustrial hosing experiments. Shown are the preindustrial control simulation (black), the 0.3 Sv hosing ensemble (green; shading indicates the five-member ensemble range), and the 0.15 Sv hosing simulation (orange; single member). The gray shading denotes ±2 standard deviations of AMOC variability in the control simulation.

Therefore, the temperature change can be distributed into six contributions:

$$\delta T = \delta T_P + \delta T_A + \delta T_W + \delta T_C + \delta T_N + \delta T_F \tag{A7}$$

Appendix B: Additional figures

Author contributions. TLF, PM, FAB, and YS designed the study. PM conducted most of the analyses with guidance from FAB, TLF, and YS. DW developed the temperature decomposition approach, which was further refined by YS. TLF led the writing of the manuscript with substantial contributions from PM. All authors contributed to the writing and revision of the manuscript.

Competing interests. All authors declare no competing interests.

Acknowledgements. This study has been supported by the Horizon Europe project TipESM "Exploring Tipping Points and Their Impacts Using Earth System Models" funded by the European Union (grant agreement no. 101137673. DOI: 10.3030/101137673, TipESM contribution no. XX) and the Bloom Foundation. The simulations were conducted at the CSCS Swiss National Supercomputing Centre for computing resources under the project s1328.

https://doi.org/10.5194/egusphere-2026-3065
Preprint. Discussion started: 24 June 2026

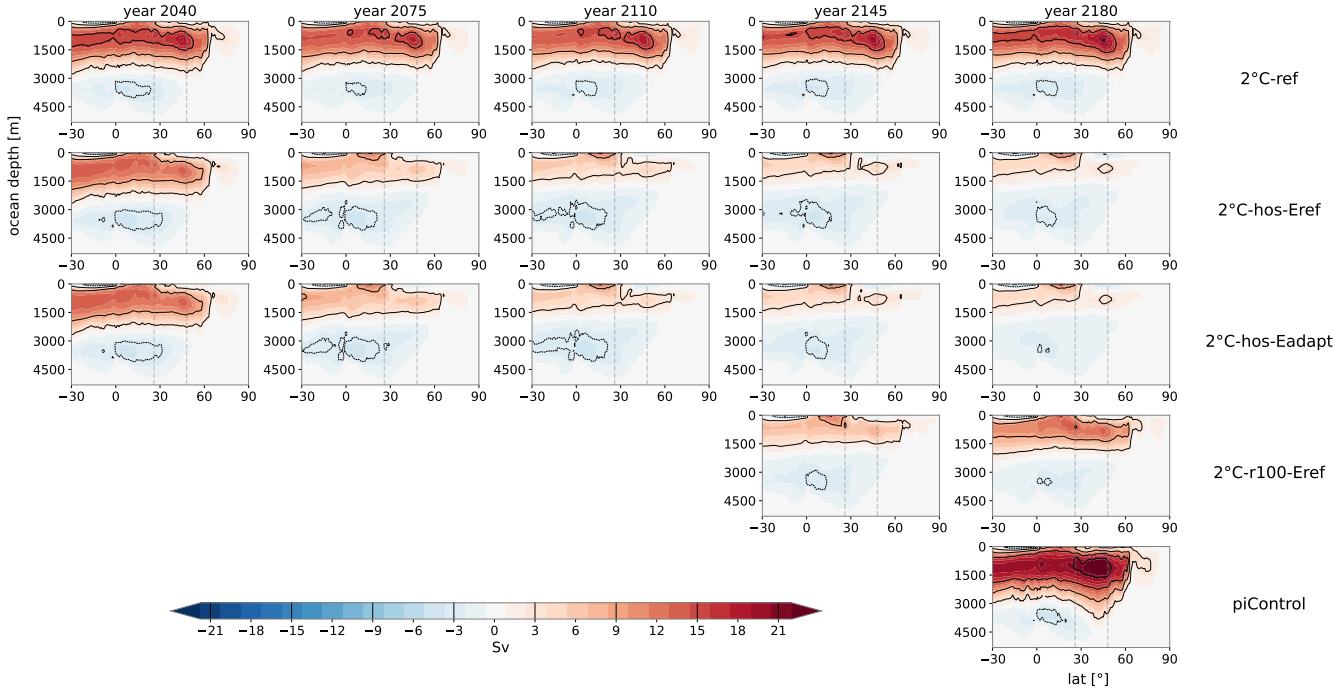

Figure B2. The meridional overturning circulation in the Atlantic Ocean, including the Arctic for different time periods and simulations. The values represent means over 30-year periods centered around the year indicated at the top of each column. The bottom row panel represents the mean over the entire preindustrial control simulation period. Each row corresponds to a different simulation scenario. The figures include vertical dashed lines at 26.5°N and 48°N.

References

Allen, M. R., Frame, D. J., Huntingford, C., Jones, C. D., Lowe, J. A., Meinshausen, M., and Meinshausen, N.: Warming Caused by Cumulative Carbon Emissions towards the Trillionth Tonne, Nature, 458, 1163–1166, https://doi.org/10.1038/nature08019, 2009.

Allen, M. R., Shine, K. P., Fuglestvedt, J. S., Millar, R. J., Cain, M., Frame, D. J., and Macey, A. H.: A Solution to the Misrepresentations of CO2-equivalent Emissions of Short-Lived Climate Pollutants under Ambitious Mitigation, npj Climate and Atmospheric Science, 1, 1–8, https://doi.org/10.1038/s41612-018-0026-8, 2018.

Anderson, Jeffrey L and Balaji, and V and Broccoli, Anthony J and Cooke, William F and Delworth, Thomas L and Dixon, Keith W and Donner, Leo J and Dunne, Krista A and Freidenreich, Stuart M and others: The New GFDL Global Atmosphere and Land Model AM2–LM2: Evaluation with Prescribed SST Simulations, Journal of Climate, 17, 4641–4673, https://doi.org/10.1175/JCLI-3223.1, 2004.

Armour, K. C., Bitz, C. M., and Roe, G. H.: Time-Varying Climate Sensitivity from Regional Feedbacks, Journal of Climate, 26, 4518–4534, https://doi.org/10.1175/JCLI-D-12-00544.1, 2013.

Arumí-Planas, C., Dong, S., Perez, R., Harrison, M. J., Farneti, R., and Hernández-Guerra, A.: A Multi-Data Set Analysis of the Freshwater Transport by the Atlantic Meridional Overturning Circulation at Nominally 34.5°S, Journal of Geophysical Research: Oceans, 129, https://doi.org/10.1029/2023jc020558, 2024.

https://doi.org/10.5194/egusphere-2026-3065
Preprint. Discussion started: 24 June 2026

Baggenstos, D., Häberli, M., Schmitt, J., Shackleton, S. A., Birner, B., Severinghaus, J. P., Kellerhals, T., and Fischer, H.: Earth's Radiative Imbalance from the Last Glacial Maximum to the Present, Proceedings of the National Academy of Sciences, 116, 14 881–14 886, https://doi.org/10.1073/pnas.1905447116, 2019.

Bellomo, K. and Mehling, O.: Impacts and State-Dependence of AMOC Weakening in a Warming Climate, Geophysical Research Letters, 51, e2023GL107 624, https://doi.org/10.1029/2023GL107624, 2024.

Ben-Yami, M., Good, P., Jackson, L. C., Crucifix, M., Hu, A., Saenko, O., Swingedouw, D., and Boers, N.: Impacts of AMOC Collapse on Monsoon Rainfall: A Multi-Model Comparison, Earth's Future, 12, e2023EF003 959, https://doi.org/10.1029/2023EF003959, 2024.

Bonnet, R., Swingedouw, D., Gastineau, G., Boucher, O., Deshayes, J., Hourdin, F., Mignot, J., Servonnat, J., and Sima, A.: Increased Risk of near Term Global Warming Due to a Recent AMOC Weakening, Nature Communications, 12, 6108, https://doi.org/10.1038/s41467-021-26370-0, 2021.

Boot, A. A., von der Heydt, A. S., and Dijkstra, H. A.: Response of Atmospheric pCO$$_2$$to a Strong AMOC Weakening under Low and High Emission Scenarios, Climate Dynamics, 62, 7559–7574, https://doi.org/10.1007/s00382-024-07295-y, 2024.

Bopp, L., Resplandy, L., Orr, J. C., Doney, S. C., Dunne, J. P., Gehlen, M., Halloran, P., Heinze, C., Ilyina, T., Séférian, R., Tjiputra, J., and Vichi, M.: Multiple Stressors of Ocean Ecosystems in the 21st Century: Projections with CMIP5 Models, Biogeosciences, 10, 6225–6245, https://doi.org/10.5194/bg-10-6225-2013, 2013.

Bozbiyik, A., Steinacher, M., Joos, F., Stocker, T. F., and Menviel, L.: Fingerprints of Changes in the Terrestrial Carbon Cycle in Response to Large Reorganizations in Ocean Circulation, Climate of the Past, 7, 319–338, https://doi.org/10.5194/cp-7-319-2011, 2011.

Broecker, W. S.: The Great Ocean Conveyor, in: AIP Conference Proceedings, vol. 247, pp. 129–161, AIP, Washington, DC (USA), ISSN 0094243X, https://doi.org/10.1063/1.41925, 1992.

Broecker, W. S.: Abrupt Climate Change Revisited, Global and Planetary Change, 54, 211–215, https://doi.org/10.1016/j.gloplacha.2006.06.019, 2006.

Bronselaer, B., Winton, M., Russell, J., Sabine, C. L., and Khatiwala, S.: Agreement of CMIP5 Simulated and Observed Ocean Anthropogenic CO2 Uptake, Geophysical Research Letters, 44, 12,298–12,305, https://doi.org/10.1002/2017GL074435, 2017.

Buckley, M. W. and Marshall, J.: Observations, Inferences, and Mechanisms of the Atlantic Meridional Overturning Circulation: A Review, Reviews of Geophysics, 54, 5–63, https://doi.org/10.1002/2015RG000493, 2016.

Burger, F. A., Terhaar, J., and Frölicher, T. L.: Compound Marine Heatwaves and Ocean Acidity Extremes, Nature Communications, 13, 4722, https://doi.org/10.1038/s41467-022-32120-7, 2022.

Caesar, L., Rahmstorf, S., Robinson, A., Feulner, G., and Saba, V.: Observed Fingerprint of a Weakening Atlantic Ocean Overturning Circulation, Nature, 556, 191–196, https://doi.org/10.1038/s41586-018-0006-5, 2018.

Campos, M. C., Chiessi, C. M., Prange, M., Mulitza, S., Kuhnert, H., Paul, A., Venancio, I. M., Albuquerque, A. L. S., Cruz, F. W., and Bahr, A.: A New Mechanism for Millennial Scale Positive Precipitation Anomalies over Tropical South America, Quaternary Science Reviews, 225, 105 990, https://doi.org/10.1016/j.quascirev.2019.105990, 2019.

Ciemer, C., Winkelmann, R., Kurths, J., and Boers, N.: Impact of an AMOC Weakening on the Stability of the Southern Amazon Rainforest, The European Physical Journal Special Topics, 230, 3065–3073, https://doi.org/10.1140/epjs/s11734-021-00186-x, 2021.

Clark, P. U., Pisias, N. G., Stocker, T. F., and Weaver, A. J.: The Role of the Thermohaline Circulation in Abrupt Climate Change, Nature, 415, 863–869, https://doi.org/10.1038/415863a, 2002.

https://doi.org/10.5194/egusphere-2026-3065
Preprint. Discussion started: 24 June 2026

Dansgaard, W., Johnsen, S. J., Clausen, H. B., Dahl-Jensen, D., Gundestrup, N. S., Hammer, C. U., Hvidberg, C. S., Steffensen, J. P., Sveinbjörnsdottir, A. E., Jouzel, J., and Bond, G.: Evidence for General Instability of Past Climate from a 250-Kyr Ice-Core Record, Nature, 364, 218–220, https://doi.org/10.1038/364218a0, 1993.

Delworth, T. L., Broccoli, A. J., Rosati, A., Stouffer, R. J., Balaji, V., Beesley, J. A., Cooke, W. F., Dixon, K. W., Dunne, J., Dunne, K. A., Durachta, J. W., Findell, K. L., Ginoux, P., Gnanadesikan, A., Gordon, C. T., Griffies, S. M., Gudgel, R., Harrison, M. J., Held, I. M., Hemler, R. S., Horowitz, L. W., Klein, S. A., Knutson, T. R., Kushner, P. J., Langenhorst, A. R., Lee, H.-C., Lin, S.-J., Lu, J., Malyshev, S. L., Milly, P. C. D., Ramaswamy, V., Russell, J., Schwarzkopf, M. D., Shevliakova, E., Sirutis, J. J., Spelman, M. J., Stern, W. F., Winton, M., Wittenberg, A. T., Wyman, B., Zeng, F., and Zhang, R.: GFDL's CM2 Global Coupled Climate Models. Part I: Formulation and Simulation Characteristics, Journal of Climate, 19, 643–674, https://doi.org/10.1175/JCLI3629.1, 2006.

Dijkstra, H. A. and Van Westen, R. M.: The Effect of Indian Ocean Surface Freshwater Flux Biases On the Multi-Stable Regime of the AMOC, Tellus A: Dynamic Meteorology and Oceanography, 76, 90–100, https://doi.org/10.16993/tellusa.3246, 2024.

Dijkstra, H. A. and van Westen, R. M.: The Probability of an AMOC Collapse Onset in the Twenty-First Century, https://doi.org/10.1146/annurev-marine-040324-024822, 2025.

Drijfhout, S.: Competition between Global Warming and an Abrupt Collapse of the AMOC in Earth's Energy Imbalance, Scientific Reports, 5, 14 877, https://doi.org/10.1038/srep14877, 2015.

Drijfhout, S., Angevaare, J. R., Mecking, J., Van Westen, R. M., and Rahmstorf, S.: Shutdown of Northern Atlantic Overturning after 2100 Following Deep Mixing Collapse in CMIP6 Projections, Environmental Research Letters, 20, 094 062, https://doi.org/10.1088/1748-9326/adfa3b, 2025.

Dunne, J. P., John, J. G., Adcroft, A. J., Griffies, S. M., Hallberg, R. W., Shevliakova, E., Stouffer, R. J., Cooke, W., Dunne, K. A., Harrison, M. J., Krasting, J. P., Malyshev, S. L., Milly, P. C. D., Phillipps, P. J., Sentman, L. T., Samuels, B. L., Spelman, M. J., Winton, M., Wittenberg, A. T., and Zadeh, N.: GFDL's ESM2 Global Coupled Climate–Carbon Earth System Models. Part I: Physical Formulation and Baseline Simulation Characteristics, Journal of Climate, 25, 6646–6665, https://doi.org/10.1175/JCLI-D-11-00560.1, 2012.

Dunne, J. P., Stouffer, R. J., and John, J. G.: Reductions in Labour Capacity from Heat Stress under Climate Warming, Nature Climate Change, 3, 563–566, https://doi.org/10.1038/nclimate1827, 2013.

Dupont, L. M., Schlütz, F., Ewah, C. T., Jennerjahn, T. C., Paul, A., and Behling, H.: Two-Step Vegetation Response to Enhanced Precipitation in Northeast Brazil during Heinrich Event 1, Global Change Biology, 16, 1647–1660, https://doi.org/10.1111/j.1365-2486.2009.02023.x, 2010.

Forster, P. M., Smith, C., Walsh, T., Lamb, W. F., Lamboll, R., Cassou, C., Hauser, M., Hausfather, Z., Lee, J.-Y., Palmer, M. D., von Schuckmann, K., Slangen, A. B. A., Szopa, S., Trewin, B., Yun, J., Gillett, N. P., Jenkins, S., Matthews, H. D., Raghavan, K., Ribes, A., Rogelj, J., Rosen, D., Zhang, X., Allen, M., Aleluia Reis, L., Andrew, R. M., Betts, R. A., Borger, A., Broersma, J. A., Burgess, S. N., Cheng, L., Friedlingstein, P., Domingues, C. M., Gambarini, M., Gasser, T., Gütschow, J., Ishii, M., Kadow, C., Kennedy, J., Killick, R. E., Krummel, P. B., Liné, A., Monselesan, D. P., Morice, C., Mühle, J., Naik, V., Peters, G. P., Pirani, A., Pongratz, J., Minx, J. C., Rigby, M., Rohde, R., Savita, A., Seneviratne, S. I., Thorne, P., Wells, C., Western, L. M., van der Werf, G. R., Wijffels, S. E., Masson-Delmotte, V., and Zhai, P.: Indicators of Global Climate Change 2024: Annual Update of Key Indicators of the State of the Climate System and Human Influence, Earth System Science Data, 17, 2641–2680, https://doi.org/10.5194/essd-17-2641-2025, 2025.

Fox-Kemper, B., Danabasoglu, G., Ferrari, R., Griffies, S. M., Hallberg, R. W., Holland, M. M., Maltrud, M. E., Peacock, S., and Samuels, B. L.: Parameterization of Mixed Layer Eddies. III: Implementation and Impact in Global Ocean Climate Simulations, Ocean Modelling, 39, 61–78, https://doi.org/10.1016/j.ocemod.2010.09.002, 2011.

https://doi.org/10.5194/egusphere-2026-3065
Preprint. Discussion started: 24 June 2026

Fox-Kemper, B., Hewitt, H., Xiao, C., Aðalgeirsdóttir, G., Drijfhout, S., Edwards, T., Golledge, N., Hemer, M., Kopp, R., Krinner, G., Mix, A., Notz, D., Nowicki, S., Nurhati, I., Ruiz, L., Sallée, J.-B., Slangen, A., and Yu, Y.: Ocean, Cryosphere and Sea Level Change, in: Climate Change 2021: The Physical Science Basis. Contribution of Working Group I to the Sixth Assessment Report of the Intergovernmental Panel on Climate Change, edited by Masson-Delmotte, V., P. Zhai, A. Pirani, S.L. Connors, C. Péan, S. Berger, N. Caud, Y. Chen, L. Goldfarb, M.I. Gomis, M. Huang, K. Leitzell, E. Lonnoy, J.B.R. Matthews, T.K. Maycock, T. Waterfield, O. Yelekçi, R. Yu, and B. Zhou, pp. 1211–1362, Cambridge University Press, 1 edn., ISBN 978-1-009-15789-6, https://doi.org/10.1017/9781009157896, 2021.

Frölicher, T. L., Sarmiento, J. L., Paynter, D. J., Dunne, J. P., Krasting, J. P., and Winton, M.: Dominance of the Southern Ocean in Anthropogenic Carbon and Heat Uptake in CMIP5 Models, Journal of Climate, 28, 862–886, https://doi.org/10.1175/JCLI-D-14-00117.1, 2015.

Frölicher, T. L., Ramseyer, L., Raible, C. C., Rodgers, K. B., and Dunne, J.: Potential Predictability of Marine Ecosystem Drivers, Biogeosciences, 17, 2061–2083, https://doi.org/10.5194/bg-17-2061-2020, 2020.

Galbraith, E. D., Merlis, T. M., and Palter, J. B.: Destabilization of Glacial Climate by the Radiative Impact of Atlantic Meridional Overturning Circulation Disruptions, Geophysical Research Letters, 43, 8214–8221, https://doi.org/10.1002/2016GL069846, 2016.

Ganachaud, A. and Wunsch, C.: Improved Estimates of Global Ocean Circulation, Heat Transport and Mixing from Hydrographic Data, Nature, 408, 453–457, https://doi.org/10.1038/35044048, 2000.

Gerber, L., Lippold, J., Süfke, F., Valk, O., Testorf, P., Ehnis, M., Tautenhahn, S., Max, L., Chiessi, C. M., Regelous, M., Szidat, S., Friedrich, O., and Pöppelmeier, F.: Low Variability of the Atlantic Meridional Overturning Circulation throughout the Holocene, Nature Communications, 16, 6748, https://doi.org/10.1038/s41467-025-61793-z, 2025.

Glaude, Q., Noel, B., Olesen, M., Van den Broeke, M., van de Berg, W. J., Mottram, R., Hansen, N., Delhasse, A., Amory, C., Kittel, C., Goelzer, H., and Fettweis, X.: A Factor Two Difference in 21st-Century Greenland Ice Sheet Surface Mass Balance Projections From Three Regional Climate Models Under a Strong Warming Scenario (SSP5-8.5), Geophysical Research Letters, 51, e2024GL111 902, https://doi.org/10.1029/2024GL111902, 2024.

Gottschalk, J., Battaglia, G., Fischer, H., Frölicher, T. L., Jaccard, S. L., Jeltsch-Thömmes, A., Joos, F., Köhler, P., Meissner, K. J., Menviel, L., Nehrbass-Ahles, C., Schmitt, J., Schmittner, A., Skinner, L. C., and Stocker, T. F.: Mechanisms of Millennial-Scale Atmospheric CO2 Change in Numerical Model Simulations, Quaternary Science Reviews, 220, 30–74, https://doi.org/10.1016/j.quascirev.2019.05.013, 2019.

Gregory, J. M., Ingram, W. J., Palmer, M. A., Jones, G. S., Stott, P. A., Thorpe, R. B., Lowe, J. A., Johns, T. C., and Williams, K. D.: A New Method for Diagnosing Radiative Forcing and Climate Sensitivity, Geophysical Research Letters, 31, 2003GL018 747, https://doi.org/10.1029/2003GL018747, 2004.

Gregory, J. M., Bloch-Johnson, J., Couldrey, M. P., Exarchou, E., Griffies, S. M., Kuhlbrodt, T., Newsom, E., Saenko, O. A., Suzuki, T., Wu, Q., Urakawa, S., and Zanna, L.: A New Conceptual Model of Global Ocean Heat Uptake, Climate Dynamics, 62, 1669–1713, https://doi.org/10.1007/s00382-023-06989-z, 2024.

Griffies, S. M., NOAA, and Laboratory, G. F. D.: ELEMENTS OF MOM4P1, GFDL OCEAN GROUP TECHNICAL REPORT NO. 6, https://doi.org/https://www.gfdl.noaa.gov/wp-content/uploads/files/model_development/ocean/guide4p1.pdf, 2009.

Griffies, S. M., Danabasoglu, G., Durack, P. J., Adcroft, A. J., Balaji, V., Böning, C. W., Chassignet, E. P., Curchitser, E., Deshayes, J., Drange, H., Fox-Kemper, B., Gleckler, P. J., Gregory, J. M., Haak, H., Hallberg, R. W., Heimbach, P., Hewitt, H. T., Holland, D. M., Ilyina, T., Jungclaus, J. H., Komuro, Y., Krasting, J. P., Large, W. G., Marsland, S. J., Masina, S., McDougall, T. J., Nurser, A. J. G., Orr, J. C., Pirani, A., Qiao, F., Stouffer, R. J., Taylor, K. E., Treguier, A. M., Tsujino, H., Uotila, P., Valdivieso, M., Wang, Q., Winton, M.,

https://doi.org/10.5194/egusphere-2026-3065
Preprint. Discussion started: 24 June 2026

and Yeager, S. G.: OMIP Contribution to CMIP6: Experimental and Diagnostic Protocol for the Physical Component of the Ocean Model Intercomparison Project, Geoscientific Model Development, 9, 3231–3296, https://doi.org/10.5194/gmd-9-3231-2016, 2016.

Heinrich, H.: Origin and Consequences of Cyclic Ice Rafting in the Northeast Atlantic Ocean During the Past 130,000 Years, Quaternary Research, 29, 142–152, https://doi.org/10.1016/0033-5894(88)90057-9, 1988.

Howard, T., Palmer, M. D., Jackson, L. C., and Yamazaki, K.: Storm Surge Changes around the UK under a Weakened Atlantic Meridional Overturning Circulation, Environmental Research Communications, 6, 035 026, https://doi.org/10.1088/2515-7620/ad3368, 2024.

IPCC AR6 WGI: Climate Change 2021 – The Physical Science Basis: Working Group I Contribution to the Sixth Assessment Report of the Intergovernmental Panel on Climate Change, Cambridge University Press, 1 edn., ISBN 978-1-009-15789-6, https://doi.org/10.1017/9781009157896, 2023.

Iturbide, M., Gutiérrez, J. M., Alves, L. M., Bedia, J., Cerezo-Mota, R., Cimadevilla, E., Cofiño, A. S., Di Luca, A., Faria, S. H., Gorodetskaya, I. V., Hauser, M., Herrera, S., Hennessy, K., Hewitt, H. T., Jones, R. G., Krakovska, S., Manzanas, R., Martínez-Castro, D., Narisma, G. T., Nurhati, I. S., Pinto, I., Seneviratne, S. I., van den Hurk, B., and Vera, C. S.: An Update of IPCC Climate Reference Regions for Subcontinental Analysis of Climate Model Data: Definition and Aggregated Datasets, Earth System Science Data, 12, 2959–2970, https://doi.org/10.5194/essd-12-2959-2020, 2020.

Jackett, D. R., McDougall, T. J., Feistel, R., Wright, D. G., and Griffies, S. M.: Algorithms for Density, Potential Temperature, Conservative Temperature, and the Freezing Temperature of Seawater, Journal of Atmospheric and Oceanic Technology, 23, 1709–1728, https://doi.org/10.1175/JTECH1946.1, 2006.

Jackson, L. C., Kahana, R., Graham, T., Ringer, M. A., Woollings, T., Mecking, J. V., and Wood, R. A.: Global and European Climate Impacts of a Slowdown of the AMOC in a High Resolution GCM, Climate Dynamics, 45, 3299–3316, https://doi.org/10.1007/s00382-015-2540-2, 2015.

Jackson, L. C., Alastrué de Asenjo, E., Bellomo, K., Danabasoglu, G., Haak, H., Hu, A., Jungclaus, J., Lee, W., Meccia, V. L., Saenko, O., Shao, A., and Swingedouw, D.: Understanding AMOC Stability: The North Atlantic Hosing Model Intercomparison Project, Geoscientific Model Development, 16, 1975–1995, https://doi.org/10.5194/gmd-16-1975-2023, 2023.

Jones, C., Bossert, I., Dennis, D. P., Jeffery, H., Jones, C. D., Koenigk, T., Loriani, S., Sanderson, B., Séférian, R., Wyser, K., Yang, S., Abe, M., Bathiany, S., Braconnot, P., Brovkin, V., Burger, F. A., Cadule, P., Castruccio, F. S., Danabasoglu, G., Dittus, A., Donges, J. F., Fröb, F., Frölicher, T., Georgievski, G., Guo, C., Hu, A., Lawrence, P., Lerner, P., Licón-Saláiz, J., Otto-Bliesner, B., Romanou, A., Shevliakova, E., Silvy, Y., Swingedouw, D., Tjiputra, J., Walton, J., Wiltshire, A., Winkelmann, R., Wood, R., Yokohata, T., and Ziehn, T.: The TIPMIP Earth System Model Experiment Protocol: Phase 1, EGUsphere, pp. 1–45, https://doi.org/10.5194/egusphere-2025-3604, 2025.

Kageyama, M., Braconnot, P., Chiessi, C. M., Rehfeld, K., Ait Brahim, Y., Dütsch, M., Gwinneth, B., Hou, A., Loutre, M.-F., Hendrizan, M., Meissner, K., Mongwe, P., Otto-Bliesner, B., Pezzi, L. P., Rovere, A., Seltzer, A., Sime, L., and Zhu, J.: Lessons from Paleoclimates for Recent and Future Climate Change: Opportunities and Insights, Frontiers in Climate, 6, https://doi.org/10.3389/fclim.2024.1511997, 2024.

Katsman, C. A. and van Oldenborgh, G. J.: Tracing the Upper Ocean's "Missing Heat", Geophysical Research Letters, 38, https://doi.org/10.1029/2011GL048417, 2011.

Knutti, R. and Stocker, T. F.: Influence of the Thermohaline Circulation on Projected Sea Level Rise, Journal of Climate, 13, 1997–2001, https://doi.org/10.1175/1520-0442(2000)013<1997:IOTTCO>2.0.CO;2, 2000.

https://doi.org/10.5194/egusphere-2026-3065
Preprint. Discussion started: 24 June 2026

Lacroix, F., Burger, F. A., Silvy, Y., Schleussner, C.-F., and Frölicher, T. L.: Persistently Elevated High-Latitude Ocean Temperatures and Global Sea Level Following Temporary Temperature Overshoots, Earth's Future, 12, e2024EF004 862, https://doi.org/10.1029/2024EF004862, 2024.

Liu, W., Xie, S.-P., Liu, Z., and Zhu, J.: Overlooked Possibility of a Collapsed Atlantic Meridional Overturning Circulation in Warming Climate, Science Advances, 3, e1601 666, https://doi.org/10.1126/sciadv.1601666, 2017.

Liu, W., Fedorov, A. V., Xie, S.-P., and Hu, S.: Climate Impacts of a Weakened Atlantic Meridional Overturning Circulation in a Warming Climate, Science Advances, 6, eaaz4876, https://doi.org/10.1126/sciadv.aaz4876, 2020.

Lynch-Stieglitz, J.: The Atlantic Meridional Overturning Circulation and Abrupt Climate Change, Annual Review of Marine Science, 9, 83–104, https://doi.org/10.1146/annurev-marine-010816-060415, 2017.

Ma, Q., Shi, X., Scholz, P., Sidorenko, D., Lohmann, G., and Ionita, M.: Revisiting Climate Impacts of an AMOC Slowdown: Dependence on Freshwater Locations in the North Atlantic, Science Advances, 10, eadr3243, https://doi.org/10.1126/sciadv.adr3243, 2024.

Manabe, S. and Stouffer, R. J.: Simulation of Abrupt Climate Change Induced by Freshwater Input to the North Atlantic Ocean, Nature, 378, 165–167, https://doi.org/10.1038/378165a0, 1995.

Matthews, H. D., Gillett, N. P., Stott, P. A., and Zickfeld, K.: The Proportionality of Global Warming to Cumulative Carbon Emissions, Nature, 459, 829–832, https://doi.org/10.1038/nature08047, 2009.

Matthews, H. D., Tokarska, K. B., Nicholls, Z. R. J., Rogelj, J., Canadell, J. G., Friedlingstein, P., Frölicher, T. L., Forster, P. M., Gillett, N. P., Ilyina, T., Jackson, R. B., Jones, C. D., Koven, C., Knutti, R., MacDougall, A. H., Meinshausen, M., Mengis, N., Séférian, R., and Zickfeld, K.: Opportunities and Challenges in Using Remaining Carbon Budgets to Guide Climate Policy, Nature Geoscience, 13, 769–779, https://doi.org/10.1038/s41561-020-00663-3, 2020.

Mcwilliams, J. C., Norton, N. J., Gent, P. R., and Haidvogel, D. B.: A Linear Balance Model of Wind-Driven, Midlatitude Ocean Circulation, Journal of Physical Oceanography, 20, 1349–1378, https://doi.org/10.1175/1520-0485(1990)020<1349:ALBMOW>2.0.CO;2, 1990.

Meccia, V. L., Simolo, C., Bellomo, K., and Corti, S.: Extreme Cold Events in Europe under a Reduced AMOC, Environmental Research Letters, 19, 014 054, https://doi.org/10.1088/1748-9326/ad14b0, 2023.

Meccia, V. L., Simolo, C., Bellomo, K., and Corti, S.: The Impact of a Weakened AMOC on European Heatwaves, Environmental Research Letters, 20, 024 005, https://doi.org/10.1088/1748-9326/ada3e7, 2025.

Menviel, L., Timmermann, A., Mouchet, A., and Timm, O.: Meridional Reorganizations of Marine and Terrestrial Productivity during Heinrich Events, Paleoceanography, 23, https://doi.org/10.1029/2007PA001445, 2008.

Moat, Ben I, Smeed, David, Rayner, Darren, Johns, William E, Smith, Ryan H, Volkov, Denis L, Elipot, Shane, Petit, Tillys, Kajtar, Jules B, Baringer, Molly O, and Collins, Julie: Atlantic Meridional Overturning Circulation Observed by the RAPID-MOCHA-WBTS (RAPID-Meridional Overturning Circulation and Heatflux Array-Western Boundary Time Series) Array at 26N from 2004 to 2023 (V2023.1a)., https://doi.org/10.5285/33826D6E-801C-B0A7-E063-7086ABC0B9DB, 2025.

Mulitza, S., Chiessi, C. M., Schefuß, E., Lippold, J., Wichmann, D., Antz, B., Mackensen, A., Paul, A., Prange, M., Rehfeld, K., Werner, M., Bickert, T., Frank, N., Kuhnert, H., Lynch-Stieglitz, J., Portilho-Ramos, R. C., Sawakuchi, A. O., Schulz, M., Schwenk, T., Tiedemann, R., Vahlenkamp, M., and Zhang, Y.: Synchronous and Proportional Deglacial Changes in Atlantic Meridional Overturning and Northeast Brazilian Precipitation, Paleoceanography, 32, 622–633, https://doi.org/10.1002/2017PA003084, 2017.

Nian, D., Bathiany, S., Ben-Yami, M., Blaschke, L. L., Hirota, M., Rodrigues, R. R., and Boers, N.: A Potential Collapse of the Atlantic Meridional Overturning Circulation May Stabilise Eastern Amazonian Rainforests, Communications Earth & Environment, 4, 470, https://doi.org/10.1038/s43247-023-01123-7, 2023.

https://doi.org/10.5194/egusphere-2026-3065
Preprint. Discussion started: 24 June 2026

Obata, A.: Climate–Carbon Cycle Model Response to Freshwater Discharge into the North Atlantic, Journal of Climate, 20, 5962–5976, https://doi.org/10.1175/2007JCLI1808.1, 2007.

Orihuela-Pinto, B., England, M. H., and Taschetto, A. S.: Interbasin and Interhemispheric Impacts of a Collapsed Atlantic Overturning Circulation, Nature Climate Change, 12, 558–565, https://doi.org/10.1038/s41558-022-01380-y, 2022.

Palter, J. B., Griffies, S. M., Samuels, B. L., Galbraith, E. D., Gnanadesikan, A., and Klocker, A.: The Deep Ocean Buoyancy Budget and Its Temporal Variability, Journal of Climate, 27, 551–573, https://doi.org/10.1175/JCLI-D-13-00016.1, 2014.

Palter, J. B., Frölicher, T. L., Paynter, D., and John, J. G.: Climate, Ocean Circulation, and Sea Level Changes under Stabilization and Overshoot Pathways to 1.5 K Warming, Earth System Dynamics, 9, 817–828, https://doi.org/10.5194/esd-9-817-2018, 2018.

Pedro, J. B., Jochum, M., Buizert, C., He, F., Barker, S., and Rasmussen, S. O.: Beyond the Bipolar Seesaw: Toward a Process Understanding of Interhemispheric Coupling, Quaternary Science Reviews, 192, 27–46, https://doi.org/10.1016/j.quascirev.2018.05.005, 2018.

Pontes, G. M. and Menviel, L.: Weakening of the Atlantic Meridional Overturning Circulation Driven by Subarctic Freshening since the Mid-Twentieth Century, Nature Geoscience, 17, 1291–1298, https://doi.org/10.1038/s41561-024-01568-1, 2024.

Portmann, V., Swingedouw, D., Khattab, O., and Chavent, M.: Observational Constraints Project a ~50% AMOC Weakening by the End of This Century, Science Advances, 12, eadx4298, https://doi.org/10.1126/sciadv.adx4298, 2026.

Rahmstorf, S.: Ocean Circulation and Climate during the Past 120,000 Years, Nature, 419, 207–214, https://doi.org/10.1038/nature01090, 2002.

Richter, K., Riva, R., and Drange, H.: Impact of Self-attraction and Loading Effects Induced by Shelf Mass Loading on Projected Regional Sea Level Rise, Geophysical Research Letters, 40, 1144–1148, https://doi.org/10.1002/grl.50265, 2013.

Romanou, A., Rind, D., Jonas, J., Miller, R., Kelley, M., Russell, G., Orbe, C., Nazarenko, L., Latto, R., and Schmidt, G. A.: Stochastic Bifurcation of the North Atlantic Circulation under a Midrange Future Climate Scenario with the NASA-GISS ModelE, Journal of Climate, 36, 6141–6161, https://doi.org/10.1175/JCLI-D-22-0536.1, 2023.

Rose, B. E. J., Armour, K. C., Battisti, D. S., Feldl, N., and Koll, D. D. B.: The Dependence of Transient Climate Sensitivity and Radiative Feedbacks on the Spatial Pattern of Ocean Heat Uptake, Geophysical Research Letters, 41, 1071–1078, https://doi.org/10.1002/2013GL058955, 2014.

Rugenstein, M. A. A., Winton, M., Stouffer, R. J., Griffies, S. M., and Hallberg, R.: Northern High-Latitude Heat Budget Decomposition and Transient Warming, Journal of Climate, 26, 609–621, https://doi.org/10.1175/JCLI-D-11-00695.1, 2013.

Rugenstein, M. A. A., Sedláček, J., and Knutti, R.: Nonlinearities in Patterns of Long-Term Ocean Warming, Geophysical Research Letters, 43, 3380–3388, https://doi.org/10.1002/2016GL068041, 2016.

Sabine, C. L., Feely, R. A., Gruber, N., Key, R. M., Lee, K., Bullister, J. L., Wanninkhof, R., Wong, C. S., Wallace, D. W. R., Tilbrook, B., Millero, F. J., Peng, T.-H., Kozyr, A., Ono, T., and Rios, A. F.: The Oceanic Sink for Anthropogenic CO2, Science, 305, 367–371, https://doi.org/10.1126/science.1097403, 2004.

Saini, H., Pontes, G., Brown, J. R., Drysdale, R. N., Du, Y., and Menviel, L.: Australasian Hydroclimate Response to the Collapse of the Atlantic Meridional Overturning Circulation Under Pre-Industrial and Last Interglacial Climates, Paleoceanography and Paleoclimatology, 40, e2024PA004 967, https://doi.org/10.1029/2024PA004967, 2025.

Schaumann, F. and Alastrué de Asenjo, E.: Weakening AMOC Reduces Ocean Carbon Uptake and Increases the Social Cost of Carbon, Proceedings of the National Academy of Sciences, 122, e2419543 122, https://doi.org/10.1073/pnas.2419543122, 2025.

Scholze, M., Knorr, W., and Heimann, M.: Modelling Terrestrial Vegetation Dynamics and Carbon Cycling for an Abrupt Climatic Change Event, The Holocene, 13, 327–333, https://doi.org/10.1191/0959683603hl625rp, 2003.

https://doi.org/10.5194/egusphere-2026-3065
Preprint. Discussion started: 24 June 2026

Séférian, R., Berthet, S., Yool, A., Palmiéri, J., Bopp, L., Tagliabue, A., Kwiatkowski, L., Aumont, O., Christian, J., Dunne, J., Gehlen, M., Ilyina, T., John, J. G., Li, H., Long, M. C., Luo, J. Y., Nakano, H., Romanou, A., Schwinger, J., Stock, C., Santana-Falcón, Y., Takano, Y., Tjiputra, J., Tsujino, H., Watanabe, M., Wu, T., Wu, F., and Yamamoto, A.: Tracking Improvement in Simulated Marine Biogeochemistry Between CMIP5 and CMIP6, Current Climate Change Reports, 6, 95–119, https://doi.org/10.1007/s40641-020-00160-0, 2020.

Shevliakova, E., Pacala, S. W., Malyshev, S., Hurtt, G. C., Milly, P. C. D., Caspersen, J. P., Sentman, L. T., Fisk, J. P., Wirth, C., and Crevoisier, C.: Carbon Cycling under 300 Years of Land Use Change: Importance of the Secondary Vegetation Sink, Global Biogeochemical Cycles, 23, https://doi.org/10.1029/2007GB003176, 2009.

Silvy, Y., Frölicher, T. L., Terhaar, J., Joos, F., Burger, F. A., Lacroix, F., Allen, M., Bernadello, R., Bopp, L., Brovkin, V., Buzan, J. R., Cadule, P., Dix, M., Dunne, J., Friedlingstein, P., Georgievski, G., Hajima, T., Jenkins, S., Kawamiya, M., Kiang, N. Y., Lapin, V., Lee, D., Lerner, P., Mengis, N., Monteiro, E. A., Paynter, D., Peters, G. P., Romanou, A., Schwinger, J., Sparrow, S., Stofferahn, E., Tjiputra, J., Tourigny, E., and Ziehn, T.: AERA-MIP: Emission Pathways, Remaining Budgets and Carbon Cycle Dynamics Compatible with 1.5 ºC and 2 ºC Global Warming Stabilization, https://doi.org/10.5194/egusphere-2024-488, 2024.

Song, F. and Zhang, G. J.: Impact of Tropical SSTs in the North Atlantic and Southeastern Pacific on the Eastern Pacific ITCZ, Journal of Climate, 30, 1291–1305, https://doi.org/10.1175/JCLI-D-16-0310.1, 2017.

Stouffer, R. J., Yin, J., Gregory, J. M., Dixon, K. W., Spelman, M. J., Hurlin, W., Weaver, A. J., Eby, M., Flato, G. M., Hasumi, H., Hu, A., Jungclaus, J. H., Kamenkovich, I. V., Levermann, A., Montoya, M., Murakami, S., Nawrath, S., Oka, A., Peltier, W. R., Robitaille, D. Y., Sokolov, A., Vettoretti, G., and Weber, S. L.: Investigating the Causes of the Response of the Thermohaline Circulation to Past and Future Climate Changes, Journal of Climate, 19, 1365–1387, https://doi.org/10.1175/JCLI3689.1, 2006.

Swingedouw, D., Braconnot, P., and Marti, O.: Sensitivity of the Atlantic Meridional Overturning Circulation to the melting from northern glaciers in climate change experiments, Geophysical Research Letters, 33, L07 711, https://doi.org/10.1029/2006GL025765, 2006.

Swingedouw, D., Bopp, L., Matras, A., and Braconnot, P.: Effect of Land-Ice Melting and Associated Changes in the AMOC Result in Little Overall Impact on Oceanic CO2 Uptake, Geophysical Research Letters, 34, https://doi.org/10.1029/2007GL031990, 2007a.

Swingedouw, D., Braconnot, P., Delecluse, P., Guilyardi, E., and Marti, O.: Quantifying the AMOC Feedbacks during a 2×CO2 Stabilization Experiment with Land-Ice Melting, Climate Dynamics, 29, 521–534, https://doi.org/10.1007/s00382-007-0250-0, 2007b.

Swingedouw, D., Mignot, J., Braconnot, P., Mosquet, E., Kageyama, M., and Alkama, R.: Impact of Freshwater Release in the North Atlantic under Different Climate Conditions in an OAGCM, Journal of Climate, 22, 6377–6403, https://doi.org/10.1175/2009JCLI3028.1, 2009.

Swingedouw, D., Jackson, L., Hu, A., Romanou, A., Laureanti, N. C., Weijer, W., Loriani, S., Otto-Bliesner, B., Abe-Ouchi, A., Almeida, L., Bellucci, A., Börner, R., Danabasoglu, G., Dennis, D. P., Devilliers, M., Drijfhout, S., Donges, J., Fröb, F., Frölicher, T. L., Gastineau, G., Goelzer, H., Guo, C., Hofmann, U., Höse, A., Jones, C., Koenigk, T., Klose, A. K., Lembo, V., Licon-Salaiz, J., Mankoff, K., Meccia, V., Melnikova, I., Mehling, O., Menviel, L., Mignot, J., Robson, J. I., Schmidt, G. A., Smith, R., Sun, Y., Trombini, I., Willeit, M., Wood, R., Wu, F., Zhaohui, L., and Winkelmann, R.: TIPMIP-OCEAN Experimental Protocol Phase 1: Tipping Dynamics of the AMOC, https://doi.org/10.5194/egusphere-2026-1698, 2026.

Taylor, K. E., Stouffer, R. J., and Meehl, G. A.: An Overview of CMIP5 and the Experiment Design, Bulletin of the American Meteorological Society, 93, 485–498, https://doi.org/10.1175/BAMS-D-11-00094.1, 2012.

Terhaar, J., Frölicher, T. L., Aschwanden, M. T., Friedlingstein, P., and Joos, F.: Adaptive Emission Reduction Approach to Reach Any Global Warming Target, Nature Climate Change, 12, 1136–1142, https://doi.org/10.1038/s41558-022-01537-9, 2022.

Thomas, F., Jens, T., Fortunat, J., and Yona, S.: Protocol for Adaptive Emission Reduction Approach (AERA) Simulations, https://doi.org/10.5281/zenodo.7473133, 2022.

https://doi.org/10.5194/egusphere-2026-3065
Preprint. Discussion started: 24 June 2026

Tokarska, K. B., Gillett, N. P., Weaver, A. J., Arora, V. K., and Eby, M.: The Climate Response to Five Trillion Tonnes of Carbon, Nature Climate Change, 6, 851–855, https://doi.org/10.1038/nclimate3036, 2016.

Trossman, D. S., Palter, J. B., Merlis, T. M., Huang, Y., and Xia, Y.: Large-scale Ocean Circulation-cloud Interactions Reduce the Pace of Transient Climate Change, Geophysical Research Letters, 43, 3935–3943, https://doi.org/10.1002/2016GL067931, 2016.

University of Potsdam and Rahmstorf, S.: Is the Atlantic Overturning Circulation Approaching a Tipping Point?, Oceanography, https://doi.org/10.5670/oceanog.2024.501, 2024.

van Westen, R. M. and Baatsen, M. L. J.: European Temperature Extremes Under Different AMOC Scenarios in the Community Earth System Model, Geophysical Research Letters, 52, e2025GL114 611, https://doi.org/10.1029/2025GL114611, 2025.

van Westen, R. M., Kliphuis, M., and Dijkstra, H. A.: Physics-Based Early Warning Signal Shows That AMOC Is on Tipping Course, Science Advances, 10, eadk1189, https://doi.org/10.1126/sciadv.adk1189, 2024.

Van Westen, R. M., Van Der Wiel, K., Falkena, S. K. J., and Selten, F.: Changing European Hydroclimate under a Collapsed AMOC in the Community Earth System Model, Hydrology and Earth System Sciences, 29, 6607–6630, https://doi.org/10.5194/hess-29-6607-2025, 2025.

Van Westen, R. M., Katsman, C. A., and Le Bars, D.: Dynamic and Steric Sea-Level Changes Due to a Collapsing AMOC in the Community Earth System Model, Ocean Science, 22, 1353–1376, https://doi.org/10.5194/os-22-1353-2026, 2026.

Vanderborght, E., van Westen, R. M., and Dijkstra, H. A.: Feedback Processes Causing an AMOC Collapse in the Community Earth System Model, Journal of Climate, 38, 5083–5102, https://doi.org/10.1175/JCLI-D-24-0570.1, 2025.

Vellinga, M. and Wood, R. A.: Global Climatic Impacts of a Collapse of the Atlantic Thermohaline Circulation, Climatic Change, 54, 251–267, https://doi.org/10.1023/A:1016168827653, 2002.

Vellinga, M. and Wood, R. A.: Impacts of Thermohaline Circulation Shutdown in the Twenty-First Century, Climatic Change, 91, 43–63, https://doi.org/10.1007/s10584-006-9146-y, 2008.

Volkov, D. L., Zhang, K., Johns, W. E., Willis, J. K., Hobbs, W., Goes, M., Zhang, H., and Menemenlis, D.: Atlantic Meridional Overturning Circulation Increases Flood Risk along the United States Southeast Coast, Nature Communications, 14, 5095, https://doi.org/10.1038/s41467-023-40848-z, 2023.

Weijer, W., Cheng, W., Garuba, O. A., Hu, A., and Nadiga, B. T.: CMIP6 Models Predict Significant 21st Century Decline of the Atlantic Meridional Overturning Circulation, Geophysical Research Letters, 47, e2019GL086 075, https://doi.org/10.1029/2019GL086075, 2020.

Wilks, D. S.: Statistical Methods in the Atmospheric Sciences, Academic Press, ISBN 978-0-12-385023-2, 2011.

Winton, M.: A Reformulated Three-Layer Sea Ice Model, Journal of Atmospheric and Oceanic Technology, 17, 525–531, https://doi.org/10.1175/1520-0426(2000)017<0525:ARTLSI>2.0.CO;2, 2000.

Winton, M., Takahashi, K., and Held, I. M.: Importance of Ocean Heat Uptake Efficacy to Transient Climate Change, Journal of Climate, 23, 2333–2344, https://doi.org/10.1175/2009JCLI3139.1, 2010.

Winton, M., Griffies, S. M., Samuels, B. L., Sarmiento, J. L., and Frölicher, T. L.: Connecting Changing Ocean Circulation with Changing Climate, Journal of Climate, 26, 2268–2278, https://doi.org/10.1175/JCLI-D-12-00296.1, 2013.

Wunderling, N., Von Der Heydt, A. S., Aksenov, Y., Barker, S., Bastiaansen, R., Brovkin, V., Brunetti, M., Couplet, V., Kleinen, T., Lear, C. H., Lohmann, J., Roman-Cuesta, R. M., Sinet, S., Swingedouw, D., Winkelmann, R., Anand, P., Barichivich, J., Bathiany, S., Baudena, M., Bruun, J. T., Chiessi, C. M., Coxall, H. K., Docquier, D., Donges, J. F., Falkena, S. K. J., Klose, A. K., Obura, D., Rocha, J., Rynders, S., Steinert, N. J., and Willeit, M.: Climate Tipping Point Interactions and Cascades: A Review, Earth System Dynamics, 15, 41–74, https://doi.org/10.5194/esd-15-41-2024, 2024.

https://doi.org/10.5194/egusphere-2026-3065
Preprint. Discussion started: 24 June 2026

Zickfeld, K., Eby, M., and Weaver, A. J.: Carbon-Cycle Feedbacks of Changes in the Atlantic Meridional Overturning Circulation under Future Atmospheric CO2, Global Biogeochemical Cycles, 22, https://doi.org/10.1029/2007GB003118, 2008.

https://doi.org/10.5194/egusphere-2026-3065
Preprint. Discussion started: 24 June 2026

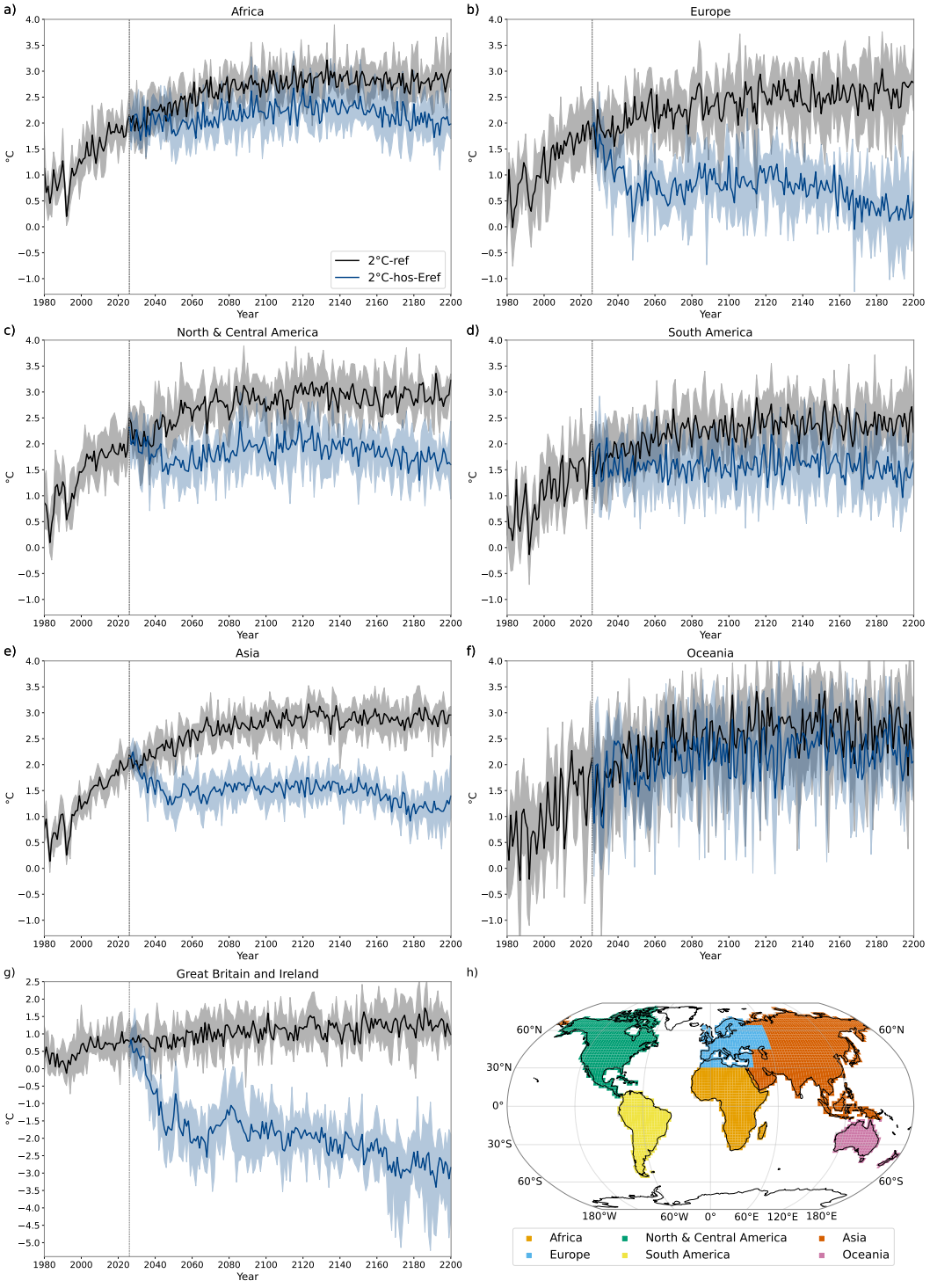

Figure B3. Annual mean surface air temperature anomalies relative to preindustrial conditions (1861–1900) for both *2°C-ref* and *2°C-hos-Eref* simulations of seven regions based on Iturbide et al. (2020). The regions (see panel h) are defined using continent names: (a) Africa, (b) Europe (combining Europe and Europe-Africa), (c) North & Central America (combining North America and Central America), (d) South America, (e) Asia, (f) Oceania, and the subregion (g) Great Britain and Ireland.

https://doi.org/10.5194/egusphere-2026-3065
Preprint. Discussion started: 24 June 2026

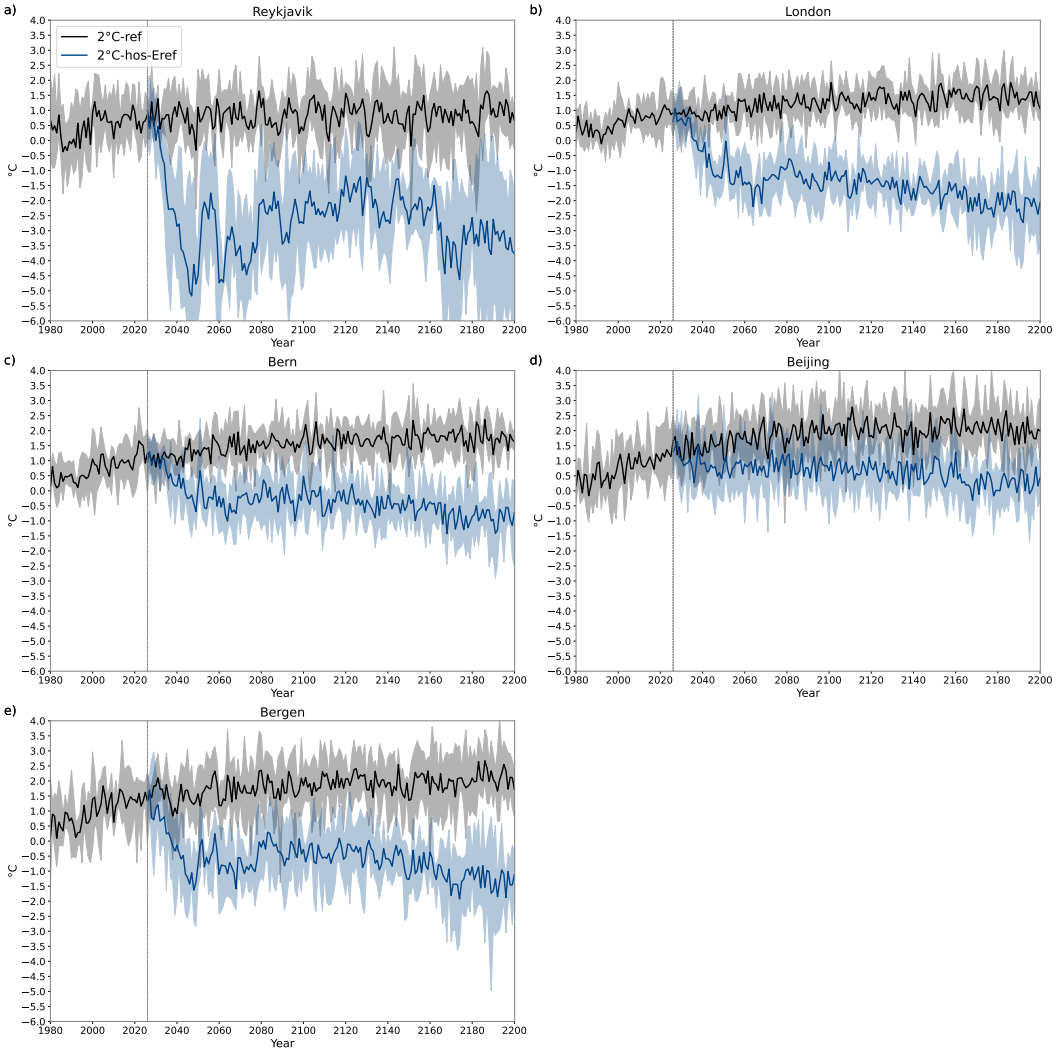

Figure B4. Annual mean surface air temperature anomalies relative to preindustrial conditions (1861–1900) for both *2°C-ref* and *2°C-hos-Eref* simulations. The red dots in Fig. 3a indicate the locations of (a) Reykjavik, (b) London, (c) Bern, (d) Beijing, and (e) Bergen.

https://doi.org/10.5194/egusphere-2026-3065
Preprint. Discussion started: 24 June 2026

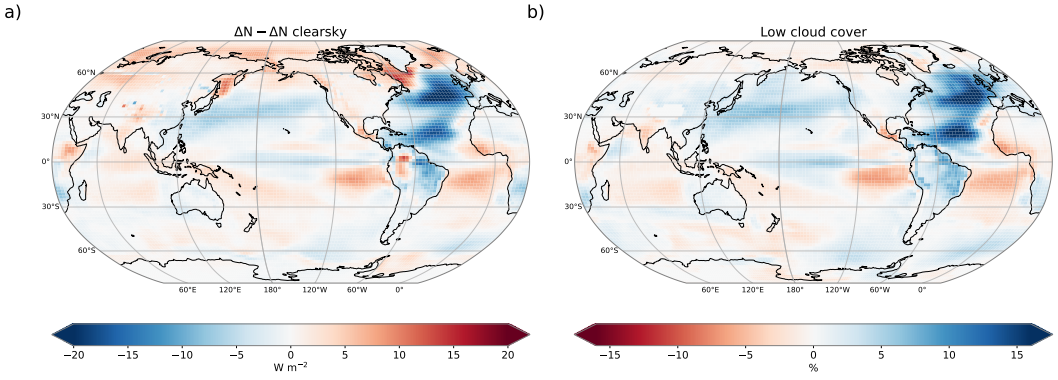

Figure B5. Spatial pattern of the 2171–2200 mean difference in (a) the change in net radiation at the top of the atmosphere (ΔN) and the change in clear-sky net radiation at top of the atmosphere ($\Delta N_{clearsky}$), and (b) low cloud cover between *2°C-hos-Eref* and *2°C-ref*

.

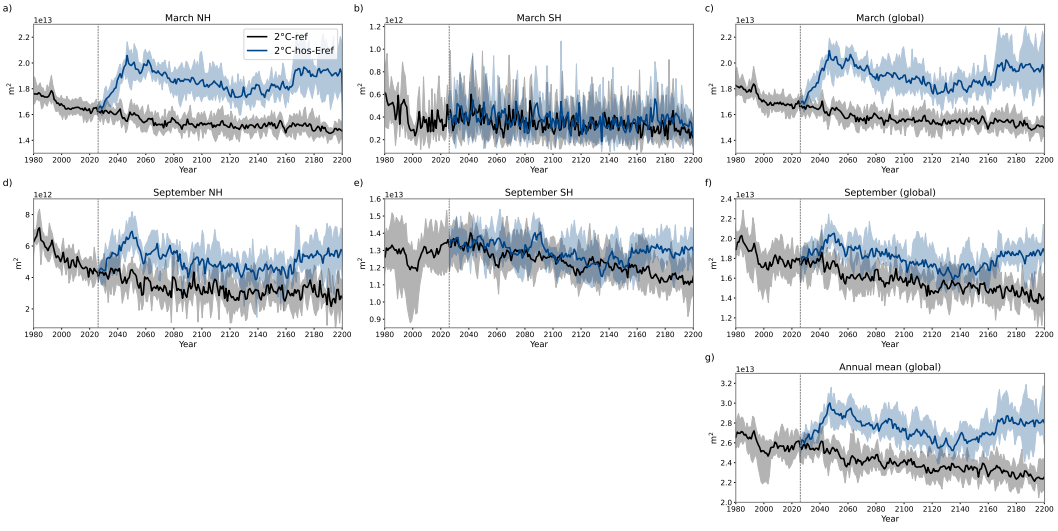

Figure B6. March, September, and annual mean sea ice extent for the Northern Hemisphere, Southern Hemisphere, and globe in the *2°C-ref* and *2°C-hos-Eref* simulations.

https://doi.org/10.5194/egusphere-2026-3065
Preprint. Discussion started: 24 June 2026

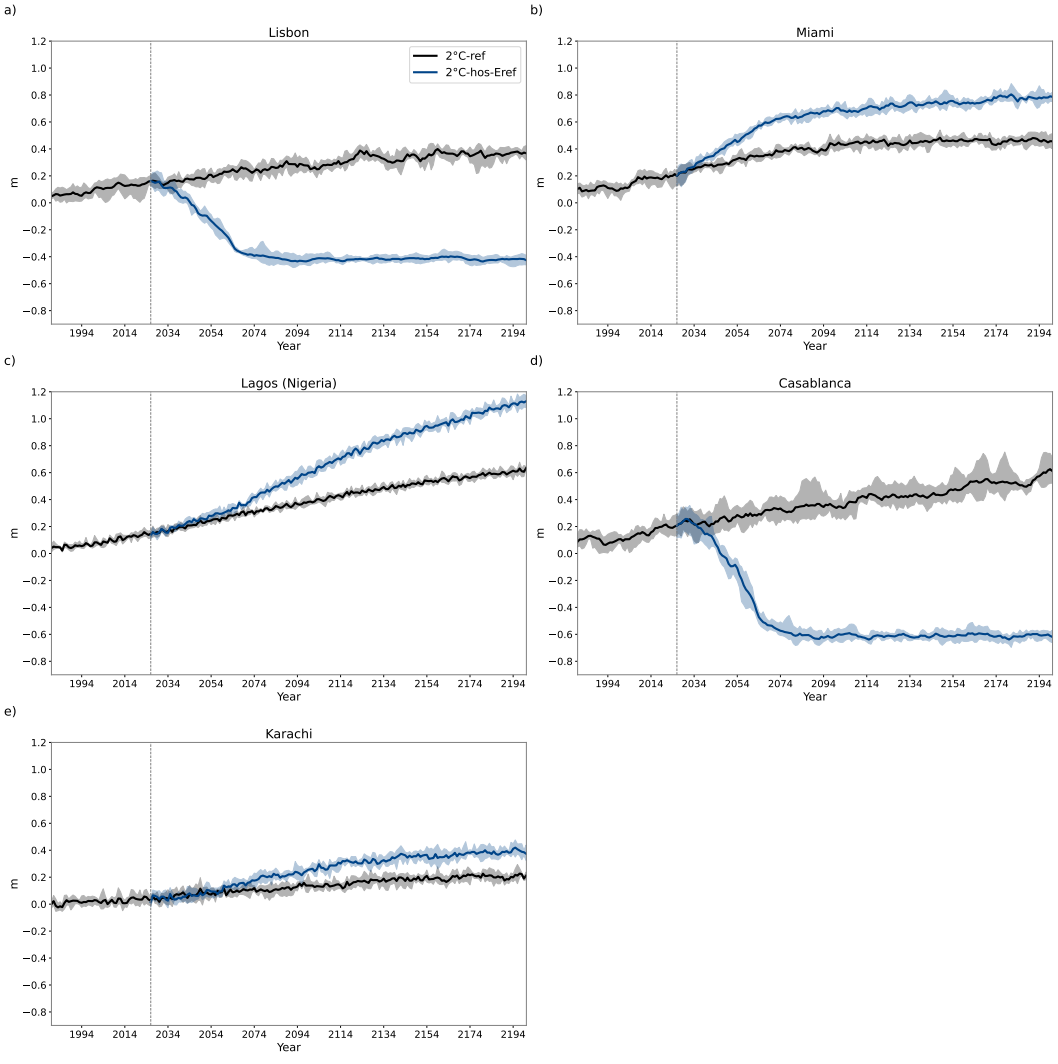

Figure B7. Thermosteric sea level rise anomalies relative to preindustrial conditions (1861–1900) for both *2°C-ref* and *2°C-hos-Eref* simulations at: (a) Lisbon, (b) Miami, (c) Lagos (Nigeria), (d) Casablanca, and (e) Karachi.

https://doi.org/10.5194/egusphere-2026-3065
Preprint. Discussion started: 24 June 2026

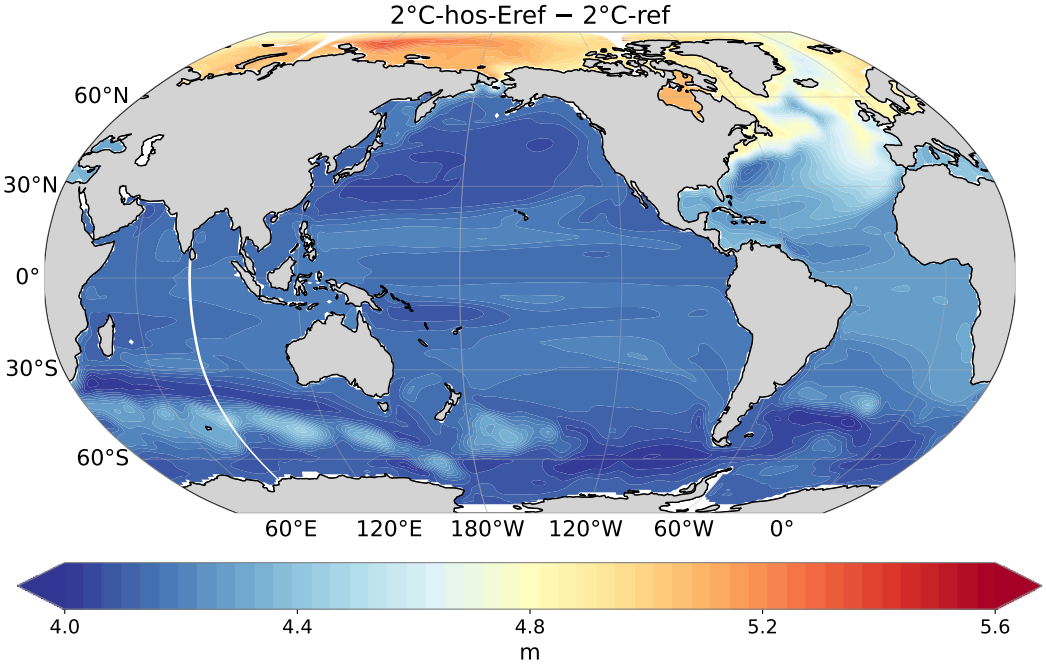

Figure B8. Spatial pattern of the 2171–2200 mean difference in dynamic sea level rise between *2°C-hos-Eref* and *2°C-ref*. Here, the dynamical sea level rise excludes the steric effect.